

1 **Single-component, self-assembling, protein nanoparticles presenting the receptor**
2 **binding domain and stabilized spike as SARS-CoV-2 vaccine candidates**

3
4 Linling He¹, Xiaohe Lin¹, Ying Wang^{4,5}, Ciril Abraham⁴, Cindy Sou¹, Timothy Ngo¹,
5 Yi Zhang^{4,5}, Ian A. Wilson^{1,3}, and Jiang Zhu^{1,2*}

6
7 ¹Department of Integrative Structural and Computational Biology, ²Department of Immunology
8 and Microbiology, ³Skaggs Institute for Chemical Biology, The Scripps Research Institute, La
9 Jolla, California 92037, USA

10
11 ⁴Fels Institute for Cancer Research and Molecular Biology, and ⁵Department of Microbiology
12 and Immunology, Temple University, Philadelphia, Pennsylvania 19140, USA.

13
14
15 * Corresponding author (to whom correspondence should be addressed)

16 JZ: Phone (858) 784-8157; Email: jiang@scripps.edu

17
18 **KEYWORDS**

19 Coronavirus disease 2019 (COVID-19); heptad repeat 2 (HR2); self-assembling protein
20 nanoparticle (SApNP); severe acute respiratory syndrome coronavirus 2 (SARS-CoV-2); spike
21 (S) protein; vaccine.

22 **ABSTRACT (150 words)**

23 Vaccination against SARS-CoV-2 provides an effective tool to combat the COVID-19 pandemic.
24 Here, we combined antigen optimization and nanoparticle display to develop vaccine candidates
25 for SARS-CoV-2. We first displayed the receptor-binding domain (RBD) on three self-
26 assembling protein nanoparticle (SAPNP) platforms using the SpyTag/SpyCatcher system. We
27 then identified heptad repeat 2 (HR2) in S2 as the cause of spike metastability, designed an HR2-
28 deleted glycine-capped spike (S2GΔHR2), and displayed S2GΔHR2 on SAPNPs. An antibody
29 column specific for the RBD enabled tag-free vaccine purification. In mice, the 24-meric RBD-
30 ferritin SAPNP elicited a more potent neutralizing antibody (NAb) response than the RBD alone
31 and the spike with two stabilizing proline mutations in S2 (S2P). S2GΔHR2 elicited two-fold-
32 higher NAb titers than S2P, while S2GΔHR2 SAPNPs derived from multilayered E2p and I3-
33 01v9 60-mers elicited up to 10-fold higher NAb titers. The S2GΔHR2-presenting I3-01v9
34 SAPNP also induced critically needed T-cell immunity, thereby providing a promising vaccine
35 candidate.

36

37 **ONE-SENTENCE SUMMARY (125 characters)**

38 The SARS-CoV-2 receptor binding domain and S2GΔHR2 spike elicited potent immune
39 responses when displayed on protein nanoparticles as vaccine candidates.

40 INTRODUCTION

41 Three coronaviruses (CoVs) have caused widespread outbreaks in humans, including severe
42 acute respiratory syndrome CoV-1 (SARS-CoV-1), Middle East respiratory syndrome CoV
43 (MERS-CoV), and SARS-CoV-2, which is the causative agent of COVID-19 (1-3) and has
44 resulted in more than 1.9 million deaths worldwide (4). Enormous efforts are being undertaken to
45 develop effective therapeutics and prophylactics for SARS-CoV-2. Small molecules that can
46 block the host receptor, angiotensin-converting enzyme 2 (ACE2), and the transmembrane
47 protease serine 2 (TMPRSS2) (5), which is required to process the spike protein, are being
48 considered as treatments in addition to other interventions (6). While the immunology underlying
49 COVID-19 is still being intensively studied (6-8), various vaccine candidates are now in clinical
50 development (9-12). Inactivated virus vaccines have exhibited robust neutralizing antibody
51 (NAb) responses in animals (13, 14), whereas viral vector vaccines based on human adenovirus
52 (Ad5 and Ad26) and chimpanzee ChAdOx1 have been evaluated in nonhuman primates (NHPs)
53 and human trials (15-18). Both DNA (19-21) and mRNA (22, 23) vaccines have been rapidly
54 developed, with moderate NAb titers observed for the mRNA vaccine in medium and high dose
55 groups (22). A recombinant spike protein adjuvanted with lipid nanoparticles (NPs), NVX-
56 CoV2373, elicited high NAb titers in a human trial that were on average four-fold greater than in
57 convalescent patients (24, 25). Efficacy was recently reported for a vector vaccine (AZD1222:
58 70.4%) (26) and two mRNA vaccines (mRNA-1273: 94.1% and BNT162b2: 95%) (27, 28). In
59 December 2020, the U.S. Food and Drug Administration (FDA) issued the emergency use
60 authorization (EUA) for the two mRNA vaccines.

61 The SARS-CoV-2 spike protein is a trimer of S1-S2 heterodimers. The S1 subunit
62 contains a receptor-binding domain (RBD) that binds to ACE2 on host cells to initiate infection.

63 The S2 subunit consists of a fusion peptide (FP) and heptad repeat regions 1 and 2 (HR1 and
64 HR2). Upon endocytosis of the virion, the S1 subunit is cleaved off to facilitate FP insertion into
65 the host cell membrane, while the remaining S2 refolds to bring HR1 and HR2 together to fuse
66 the viral and host cell membranes (29). The spike protein harbors all NAb epitopes and is the
67 main target for vaccine development against SARS-associated CoVs (30). Convalescent plasma
68 (CP) has been used to treat COVID-19 patients with severe conditions (31), highlighting the
69 importance of NAbs in protection (32). Due to moderate sequence conservation of the RBDs
70 (~73%), some previously identified NAbs targeting the SARS-CoV-1 RBD have been shown to
71 bind and cross-neutralize SARS-CoV-2 (33, 34). Using single-cell technologies and the SARS-
72 CoV-2 RBD or spike as bait, potent NAbs have now been isolated from COVID-19 patients (35-
73 41). Camelid-derived single-chain NAbs have also been obtained by panning naïve or immune
74 llama single-chain antibody (VHH) libraries (42, 43). Structures of the SARS-CoV-2 spike and
75 RBD in unliganded (44, 45), ACE2-bound (46-48), and antibody-bound (49-51) states
76 determined by x-ray crystallography and cryo-electron microscopy (cryo-EM) have paved the
77 way for rational vaccine design. Cryo-EM and cryo-electron tomography (ET) have revealed the
78 inherent spike metastability and the co-existence of pre/post-fusion spikes on virions (52). A
79 double-proline mutation (52) has been used in most soluble spike (S2P) constructs and all but
80 inactivated vaccines, although a HexaPro version with greater yield and stability is now available
81 (53). Cryo-ET has also uncovered a dynamic, triple-hinged HR2 stalk that facilitates viral entry
82 and immune evasion (54-56).

83 In this study, we designed and optimized SARS-CoV-2 antigens for multivalent display
84 on self-assembling protein nanoparticles (SApNPs) (57-59), including a ferritin (FR) 24-mer and
85 two 60-mers (E2p and I3-01) containing an inner layer of locking domains (LD) and a cluster of

86 T-cell epitopes (60). To facilitate tag-free vaccine purification, we developed an immunoaffinity
87 column based on antibody CR3022 that binds to both SARS-CoV-1/2 RBDs (34, 50). We first
88 designed a scaffolded RBD trimer construct to mimic the “RBD-up” spike conformation. The
89 SARS-CoV-1/2 RBDs were attached to SApNPs using the SpyTag/SpyCatcher system (61),
90 providing a robust strategy for developing RBD-based nanoparticle vaccines. We then probed
91 the spike metastability by comparing two uncleaved spike antigens, S2P (K986P/V987P) and
92 S2G (K986G/V987G). The SARS-CoV-2 S2G spike exhibited abnormal behavior, suggesting
93 that an unidentified facet of the spike can promote conformational change and block antibody
94 access to the RBD. An HR2-deleted spike, S2G Δ HR2, produced high-purity trimers, suggesting
95 that the HR2 stalk may be a trigger of spike metastability consistent with recent findings (54-56).
96 We next displayed S2G Δ HR2 on three SApNPs by gene fusion, resulting in spike SApNPs with
97 high yield, purity, and antigenicity. In mouse immunization, the S2P spike protein elicited the
98 lowest level of NAb response. In contrast, the scaffolded RBD trimer registered two-to-three-
99 fold higher NAb titers, with another five-fold increase in NAb titer achieved by multivalent
100 display on FR. S2G Δ HR2 elicited up to seven-fold higher NAb titers, while the large,
101 multilayered S2G Δ HR2 E2p and I3-01 SApNPs induced up-to-10-fold higher NAb titers than
102 S2P. Further analysis indicated that the S2G Δ HR2-presenting I3-01v9 SApNP can elicit a strong
103 Th1 response as well as other types of T-cell responses needed for protective cellular immunity.
104 Our study thus identifies the HR2 stalk as a major source of spike metastability, validates an
105 HR2-deleted spike design, and provides a set of RBD- and spike-based virus-like particles
106 (VLPs) as effective protein vaccine candidates against SARS-CoV-2.

107 **RESULTS**

108 **Rational design of scaffolded RBD trimers and RBD-presenting SApNPs**

109 RBD binding to the ACE2 receptor initiates the membrane fusion process (5). The crystal
110 structure of SARS-CoV-2 RBD/ACE2 complex revealed the atomic details of receptor
111 recognition (62). The SARS-CoV-2 RBD has been used as bait to isolate monoclonal antibodies
112 (mAbs) from patient samples (35-41). For SARS-CoV-1 and MERS-CoV, RBD-based vaccines
113 have induced potent NAbs that effectively block viral entry (30). Therefore, the RBD represents
114 a major target for humoral responses following infection and can be used to develop epitope-
115 focused vaccines.

116 We first hypothesized that RBD attached to a trimeric scaffold could mimic the “RBD-
117 up” spike conformation and elicit NAbs that block ACE2 binding. To test this possibility, we
118 designed a fusion construct containing SARS-CoV-1/2 RBD, a short 5-aa G₄S linker (with a 2-aa
119 restriction site), and a trimeric viral capsid protein, SHP (PDB: 1TD0) (**Fig. 1A**). Structural
120 modeling showed that the three tethered RBDs form a triangle of 92 Å (measured at L492),
121 which is 14 and 18 Å wider than the SARS-CoV-1 “two-RBD-up” spike (PDB: 6CRX, measured
122 at L478) (63) and the MERS-CoV “all-RBD-up” spike (PDB: 5X59, measured for L506) (64),
123 respectively, allowing NAb access to each RBD. We then developed an immunoaffinity
124 chromatography (IAC) column to facilitate tag-free purification. Previously, NAb-derived IAC
125 columns have been used to purify HIV-1 Env trimers/NPs (58, 59, 65, 66), hepatitis C virus
126 (HCV) E2 cores/NPs (57), and Ebola virus (EBOV) GP trimers/NPs (60). Tian et al. reported
127 that a SARS-CoV-1 NAb, CR3022, can bind SARS-CoV-2 RBD (34). The SARS-CoV-2
128 RBD/CR3022 structure revealed a conserved cryptic epitope that is shared by the two SARS-
129 CoVs, suggesting that transient breathing motions of the spike protein enabled CR3022 binding
130 to the RBD (50). Here, we examined the utility of CR3022 in IAC columns. The SARS-CoV-1/2
131 RBD-5GS-1TD0 constructs were transiently expressed in 100-ml ExpiCHO cells and purified on

132 a CR3022 column prior to size-exclusion chromatography (SEC) using a Superdex 200 10/300
133 GL column. While the SARS-CoV-1 RBD construct showed both aggregate (~8.6 ml) and trimer
134 (~12.7 ml) peaks in the SEC profile, the SARS-CoV-2 RBD construct produced a single, pure
135 trimer peak at ~12.8 ml (**Fig. 1B**). In sodium dodecyl sulfate-polyacrylamide gel electrophoresis
136 (SDS-PAGE), a monomer band of ~37 kD and a trimer band of ~100 kD were observed under
137 reducing and non-reducing conditions, respectively (**fig. S1A**). Antigenicity was assessed for the
138 two scaffolded RBD trimers in enzyme-linked immunosorbent assay (ELISA) after CR3022/SEC
139 purification (**Fig. 1C**). RBD-specific NAbs targeting SARS-CoV-1 (CR3022 (67), m396 (68),
140 80R (69), and S230 (70)) and SARS-CoV-2 (B38 (38), CB6 (37), S309 from a SARS survivor
141 (33), and P2B-2F6 (36)), were tested in ELISA. Overall, similar half maximal effective
142 concentration (EC_{50}) values were observed for the two RBD trimers binding to their respective
143 NAbs (**Fig. 1C**). The SARS-CoV-1 RBD trimer showed greater affinity for CR3022 than its
144 SARS-CoV-2 counterpart with a 1.3-fold difference in EC_{50} values, consistent with previous
145 findings (34, 50). Of the SARS-CoV-2 NAbs, B38 yielded a similar EC_{50} value to CR3022,
146 which can bind but not neutralize SARS-CoV-2. Antibody binding kinetics was measured by
147 biolayer interferometry (BLI) (**Fig. 1D** and **fig. 1B**). Overall, all tested mAbs exhibited a fast on-
148 rate, but with visible differences in their off-rates. B38 showed a faster off-rate than other SARS-
149 CoV-2 NAbs, while CR3022, the mAb used to purify SARS-CoV-1/2 RBD proteins, exhibited a
150 comparable kinetic profile.

151 We then hypothesized that the SpyTag/SpyCatcher (termed SPY) system could be used to
152 conjugate RBD to SApNPs to create multivalent RBD vaccines capable of eliciting a more
153 potent NAb response (**Fig. 1E**). The 13-aa SpyTag spontaneously reacts with the SpyCatcher
154 protein to form an irreversible isopeptide bond (61). The SPY system has been successfully used

155 to attach antigens to VLPs (71). Here, SpyTag was fused to the C terminus of RBD, while
156 SpyCatcher was fused to the N terminus of an SApNP subunit, both with a 5-aa G₄S linker. This
157 design was first tested for the 24-meric ferritin (FR). Here, we compared two production
158 strategies, co-expression of RBD-5GS-SpyTag and SpyCatcher-5GS-FR versus supernatant mix
159 after separate expression, both followed by purification on a CR3022 column. Protein obtained
160 from transient transfection in 50-ml ExpiCHO cells was analyzed by SEC on a Superose 6
161 10/300 GL column (**Fig. 1F**). Both production strategies produced a peak (12 ml) corresponding
162 to SApNPs. While the SARS-CoV-2 construct outperformed its SARS-CoV-1 counterpart in
163 particle yield (0.6-1.0 mg versus 0.3-0.5 mg after CR3022/SEC), the supernatant mix appeared to
164 be superior to co-expression for yield in both cases. The results thus suggest that both strategies
165 can be used to produce RBD SApNPs in Chinese hamster ovary (CHO) cells in an industrial
166 setting, as this mammalian expression system has been widely used to manufacture therapeutic
167 glycoproteins under good manufacturing practice (GMP) conditions (72, 73). Antigenicity was
168 assessed for SEC-purified RBD-5GS-SPY-5GS-FR SApNPs. In ELISA, RBD SApNPs showed
169 slightly improved mAb binding compared to the RBD trimers, as indicated by EC₅₀ values (**Fig.**
170 **1G**). In BLI, a more pronounced effect of multivalent display on antigenicity was observed,
171 showing notably increased binding signals and plateaued dissociation (**Fig. 1H** and **fig. 1C**).
172 Structural integrity of various RBD SApNPs was analyzed by negative stain EM (nsEM) (**Figs.**
173 **1I** and **1J**). For SARS-CoV-1, a genetically fused RBD-10GS-FR construct produced very few,
174 albeit highly pure, SApNPs (**Fig. 1I**, left). In contrast, the RBD-5GS-SPY-5GS-FR construct
175 produced a high yield of SApNPs with visible surface decorations (**Fig. 1I**, right). For SARS-
176 CoV-2, the purified RBD-5GS-SPY-5GS-FR SApNPs, irrespective of the production strategy,
177 showed morphology of well-formed particles (**Fig. 1J**). Previously, we genetically fused a small

178 LD protein and a T-cell epitope to each subunit of the E2p and I3-01v9 60-mers, resulting in
179 “multilayered” SApNPs (60). PADRE, a 13-aa pan-DR epitope that activates CD4⁺ T cells (74),
180 was used to promote B cell development toward NABs. Here, two of the best designs, E2p-LD4-
181 PADRE (or E2p-L4P) and I3-01v9-LD7-PADRE (or I3-01v9-L7P), were tested for their ability
182 to display SARS-CoV-1/2 RBDs. Following the strategy established for FR, SARS-CoV-1/2
183 RBDs were attached to the I3-01v9-L7P SApNP using the SPY system (**Fig. 1K**). Despite the
184 modest yield in ExpiCHO cells (**Fig. 1L**), large and pure particles were observed in the EM
185 images (**Fig. 1M**). However, some impurities were noted for the RBD-presenting E2p-L4P
186 SApNPs (**fig. S1D**). Nonetheless, we illustrated the utility of the SPY system for rapid
187 development of SARS-CoV-1/2 RBD vaccines based on three different SApNP platforms.

188 Recently, RBDs were displayed on various SApNPs using the SPY system as MERS-
189 CoV and SARS-CoV-2 vaccine candidates (75, 76). Walls et al. also reported a SARS-CoV-2
190 RBD vaccine candidate based on the two-component NP platform (77), which requires a
191 “connector” component to facilitate NP assembly (78), likely resulting in suboptimal stability.
192 Additionally, all these vaccine candidates require a complex production process involving two
193 expression systems, separate purification steps, and an *in vitro* assembly step before final
194 purification. In contrast, our SPY-linked RBD SApNPs are single-component by nature and can
195 be produced in CHO cells with a simple purification scheme, offering unique advantages in
196 stability and manufacturability.

197 **Rational design of prefusion spike through minimizing metastability**

198 In addition to the RBD, the SARS-CoV-1/2 spikes contain other NAb epitopes (30), which are
199 all presented in a trimeric context (**Fig. 2A**). A double-proline mutation (2P) between HR1 and
200 the central helix (CH) has been used to stabilize the MERS-CoV (79) and SARS-CoV-1 spikes

201 (63). A similar 2P mutation (K986P/V987P) was introduced into the SARS-CoV-2 spike (termed
202 S2P), which has been used to isolate and characterize NAbs (33, 35, 40, 42-45, 49) and is the
203 antigen in almost all vaccine candidates in clinical development (11, 12). However, a recent
204 cryo-EM study revealed an unexpected packing of S1 in the S2P spike, positioned ~12 Å
205 outwards, compared to the full-length native spike, as well as a more ordered FP proximal region
206 (FPPR) in S2 (52). New designs have been generated to control the spike conformation (80) or to
207 further stabilize it with more prolines (HexaPro) (53). Recent cryo-EM and cryo-ET studies
208 revealed that the SARS-CoV-2 spikes could adopt diverse orientations on native virions due to
209 the highly flexible HR2 stalk (54-56). Previously, we identified an HR1 bend as the cause of
210 HIV-1 Env metastability (58, 81) and examined the role of an equivalent HR1 bend and the HR2
211 stalk in EBOV GP metastability (60). This understanding of metastability proved critical for
212 designing stable trimers and trimer-presenting SApNP vaccines for both viruses (58-60, 81). It is
213 therefore imperative to explore the cause(s) of spike metastability to facilitate rational vaccine
214 design for SARS-CoV-2.

215 We first created uncleaved spike ectodomain (S_{ECTO}) constructs for SARS-CoV-1/2, both
216 containing the 2P mutation (K968P/V969P and K986P/V987P, respectively), a 5-aa G_4S linker, a
217 trimerization motif (PDB: 1TD0), and a C-terminal His_6 tag. The two constructs were transiently
218 expressed in 50-ml ExpiCHO cells followed by purification on either a Nickel column or a
219 CR3022 column. The $S2P_{\text{ECTO}}\text{-}5\text{GS}\text{-}1\text{TD0}\text{-}\text{His}_6$ protein was characterized by SEC on a Superose
220 6 10/300 GL column (**Fig. 2B**, panels 1 and 2). After the Nickel column, both $S2P_{\text{ECTO}}$
221 constructs showed a trimer peak (~12 ml) with the left and right shoulders indicative of
222 aggregate and dimer/monomer species, respectively. CR3022 purification resulted in a consistent
223 trimer peak, as well as reduction in dimer/monomer species. We then compared a pair of S_{ECTO}

224 constructs for SARS-CoV-1/2, both containing a double glycine (2G) mutation, K968G/V969G
225 and K986G/V987G, respectively. The 2G mutation had little effect on the SARS-CoV-1 spike
226 but produced abnormal SEC profiles and showed no yield for the SARS-CoV-2 spike after
227 purification by Nickel and CR3022 columns, respectively (**Fig. 2B**, panels 3 and 4). Lastly, we
228 tested a pair of S2G constructs without the HR2 stalk (E1150-Q1208), termed S2G Δ HR2.
229 Deletion of the HR2 stalk restored the SARS-CoV-2 trimer peak and reduced aggregates for both
230 SARS-CoV-1/2, as shown by the SEC profiles upon CR3022 purification (**Fig. 2B**, panel 5).
231 Since the triple-hinged HR2 stalk can generate diverse spike orientations on native virions (54-
232 56), and the fusion core is formed by HR1 and HR2, we hypothesized that HR2 may be a key
233 determinant of SARS-CoV-2 spike metastability (**Fig. 2C**, left). It is plausible that the
234 interactions between HR1 and HR2 of two neighboring spikes may facilitate the pre-to-post-
235 fusion transition in addition to ACE2 binding and S1 dissociation. Given the extensive sequence
236 difference in HR1 (9 amino acids in total) compared to SARS-CoV-1 (**Fig. 2C**, right), we sought
237 to examine the contribution of HR1 to SARS-CoV-2 spike metastability with two HR1-swapped
238 (HR1_s) spike constructs. Interestingly, while HR1 swapping proved ineffective, deletion of the
239 HR2 stalk once again restored the trimer peak, suggesting a more important role for HR2 (**fig.**
240 **S2, A to C**). Therefore, S2G Δ HR2 appeared to be a general spike design for SARS-CoV-1/2 and
241 perhaps other CoVs. Four separate production runs of SARS-CoV-2 S2G Δ HR2-5GS-1TD0 in
242 300-ml ExpiCHO cells resulted in nearly identical SEC profiles with trimer yields of 0.8-1.0 mg
243 (**Fig. 2D**, left). Consistently, blue native polyacrylamide gel electrophoresis (BN-PAGE) showed
244 high trimer purity across SEC fractions (**Fig. 2D**, right). Antigenicity was assessed for
245 CR3022/SEC-purified SARS-CoV-2 S2P_{ECTO} and S2G Δ HR2 spike proteins. In ELISA, the
246 S2G Δ HR2 spike showed slightly higher affinity for the five representative mAbs than did the

247 S2P_{ECTO} spike (**Fig. 2E**). When tested against three newly identified human NAbS, C105 (49)
248 and CC12.1/CC12.3 (41), the two spikes yielded similar EC₅₀ values (**fig. S2D**). In BLI, the
249 S2GΔHR2 spike showed higher binding signals than the S2P_{ECTO} spike at the highest
250 concentration, while exhibiting similar binding kinetics (**Fig. 2F**). The use of NAb P2B-2F6 (36)
251 for spike purification resulted in higher trimer yield with similar purity to the CR3022 column
252 across SEC fractions (**fig. S2E**). Thermostability was assessed by differential scanning
253 calorimetry (DSC) for CR3022/SEC-purified SARS-CoV-2 S2P_{ECTO} and S2GΔHR2 spikes (**fig.**
254 **S2F**). Upon the 2P-to-2G substitution and HR2 deletion, a small increase in thermal denaturation
255 midpoint (T_m) was observed (46.8 vs. 47.6 °C), with notably higher onset temperature (T_{on}), 35.2
256 vs. 40.0 °C, and narrower half width of the peak (ΔT_{1/2}), 4.7 vs. 3.9 °C. Altogether, we
257 demonstrated that the HR2 stalk is a major source of spike metastability and S2GΔHR2 presents
258 an alternative spike design to S2P, although more stabilizing mutations may be required to
259 achieve greater thermostability.

260 **Rational design of single-component self-assembling spike nanoparticles**

261 Although it was possible to conjugate trimeric SARS-CoV-2 spikes to an SApNP using the SPY
262 system (82), the random, irreversible linking will likely result in irregular display with
263 unoccupied but spatially occluded anchoring sites on the surface. The SPY system is perhaps
264 more suitable for small individual antigens (e.g. the RBD). Using the gene fusion approach, we
265 previously designed single-component SApNPs displaying stabilized HIV-1 Env trimers (58, 59)
266 and optimized HCV E2 cores (57). Recently, we reengineered E2p and I3-01v9 60-mers to
267 incorporate an inner layer of LDs to stabilize the non-covalently formed NP shell, in addition to
268 a cluster of T-cell epitopes (60). This multilayered design may be essential to the stability of

269 resulting SApNP vaccines when they are used to display large, complex viral antigens such as
270 the SARS-CoV-2 spike.

271 Native SARS-CoV-2 virions present both pre- and post-fusion spikes (52, 54, 55) (**Fig.**
272 **3A**, top), while our vaccine strategy aims to develop single-component SApNPs that each
273 present 8 or 20 stable prefusion S2GΔHR2 spikes to the immune system (**Fig. 3A**, bottom). As
274 demonstrated in our previous studies (58, 59), different linker lengths may be needed to connect
275 a trimer to the SApNP surface, as the spacing between the N termini of NP subunits around each
276 three-fold axis varies: FR (20 Å), E2p (9 Å), and I3-01v9 (50.5 Å). Based on this consideration,
277 we displayed the S2GΔHR2 spike on FR with a 5-aa G₄S linker, on E2p with a 5-aa G₄S linker,
278 and on I3-01v9 with a 10-aa (G₄S)₂ linker, resulting in SApNPs with diameters of 47.9, 55.9, and
279 59.3 nm, respectively (**Fig. 3B**). The multilayered E2p-L4P and I3-01v9-L7P (60), which were
280 validated for presenting RBDs (**Fig. 1, K to L; fig. S1D**), were used here as NP carriers of the
281 S2GΔHR2 spike. Together, three S2GΔHR2 SApNP constructs were transiently expressed in
282 400-ml ExpiCHO cells, followed by CR3022 purification and SEC on a Superose 6 10/300 GL
283 column (**Fig. 3C**). Three production runs for each of the three constructs generated highly
284 consistent SEC profiles, despite the variation of low molecular weight (m.w.) impurities
285 observed for the FR and E2p-L4P. After CR3022 and SEC purification, we obtained 0.3-0.4, 0.5-
286 1.0, and 0.8-1.2 mg protein for S2GΔHR2-5GS-FR, S2GΔHR2-5GS-E2p-L4P, and S2GΔHR2-
287 10GS-I3-01v9-L7P, respectively. Overall, the I3-01v9-derived S2GΔHR2 SApNP appeared to
288 perform best in terms of particle yield, purity, and stability. The structural integrity was analyzed
289 by nsEM, which showed well-formed particles of 45-65 nm with recognizable protrusions on the
290 surface (**Fig. 3D**). The varying shape of these profusions may correspond to S2GΔHR2 spikes
291 with “open” RBDs, in contrast to an array of “closed” HIV-1 and EBOV trimers on the SApNP

292 surface (58-60). Such open conformation may facilitate induction of a strong RBD-specific NAB
293 response *in vivo*. Antigenicity of S2GΔHR2 SApNPs was assessed using the same panel of
294 mAbs. In ELISA, three SApNPs showed slightly improved binding to some, but not all, mAbs
295 compared to the individual spike (**Fig. 3E**). In BLI, we observed a clear correlation between peak
296 mAb binding signal and antigen valency, with E2p/I3-01v9 > FR > spike (**Fig. 3F**). Multivalent
297 display on the two 60-mers substantially increased mAb binding compared to the FR 24-mer. In
298 previous studies, we observed a similar correlation for HIV-1 Env trimer and HCV E2 core
299 versus their SApNPs (57, 58). In summary, these VLP-size SApNPs with 8 or 20 spikes on the
300 surface provide promising vaccine candidates for *in vivo* evaluation.

301 **SARS-CoV-1/2 vaccine-induced binding antibody response**

302 Selected SARS-CoV-1/2 RBD- and spike-based vaccine constructs were assessed in BALB/c
303 mice (**Fig. 4A**). We adopted a similar immunization protocol to be consistent with our previous
304 studies on HIV-1, HCV, and EBOV SApNPs (57, 58, 60). Briefly, groups of five mice were
305 immunized four times at three-week intervals. All antigens (50 µg per dose) were formulated
306 with AddaVax, an oil-in-water emulsion adjuvant, except for I3-01v9, which was mixed with
307 aluminum phosphate (AP) (83). We first analyzed the binding antibody (bAb) responses, as
308 measured by EC₅₀ titers, in the two SARS-CoV-2 RBD vaccine groups (**Fig. 4B** and **fig. S4**).
309 The SPY-linked RBD SApNP (RBD-5GS-SPY-5GS-FR) elicited significantly higher bAb titers
310 than the scaffolded RBD trimer (RBD-5GS-1TD0) at w2 and w5, irrespective of the coating
311 antigen, and yielded a significant *P* value at w8 when the RBD was coated. Compared to the
312 S2P_{ECTO} spike (S2P_{ECTO}-5GS-1TD0), the RBD SApNP elicited significantly higher bAb titers
313 against the RBD at w2, w5, and w8 (**Fig. 4B**, right), demonstrating a strong epitope-focusing
314 effect. Mouse sera bound the SARS-CoV-1 spike with lower EC₅₀ titers than the SARS-CoV-2

315 spike but with similar patterns (**fig. S4A**). We then analyzed the bAb responses induced by
316 SARS-CoV-2 spikes S2P_{ECTO}-5GS-1TD0 and S2GΔHR2-5GS-1TD0, as well as three SApNPs
317 each displaying 8 or 20 S2GΔHR2 spikes (**Fig. 4C** and **fig. S5**). The S2GΔHR2 spike showed
318 two-three-fold higher average EC₅₀ titers than the S2P_{ECTO} spike irrespective of the coating
319 antigen (of note, to facilitate a fair comparison, mouse sera from these two groups were tested
320 against their respective spike antigens). Three SApNPs exhibited different temporal patterns
321 depending on the coating antigen. In terms of spike-specific response, the I3-01v9 group
322 registered a steady increase in average EC₅₀ titer over time, showing the highest bAb titers at w2
323 and w8 and significantly outperforming the S2P_{ECTO} group at all time points. The I3-01v9 group
324 also yielded higher EC₅₀ titers than the S2GΔHR2 group throughout, although not with
325 significant *P* values. The FR SApNP group exhibited a similar temporal pattern with lower EC₅₀
326 titers, which were still significantly higher than the S2P_{ECTO} group. Among the three SApNPs,
327 E2p exhibited the lowest average EC₅₀ titer at w2 and reached the highest at w5, which then
328 decreased slightly at w8. In terms of RBD-specific response, the five groups showed a clear
329 ranking based on their average EC₅₀ titers, which remained consistent across time points. At w2,
330 I3-01v9 showed an average EC₅₀ titer of 175, whereas all other spike-based vaccines induced
331 little RBD-specific bAb response. At w5 and w8, S2GΔHR2 elicited higher bAb titers (on
332 average by two-fold) than S2P_{ECTO}, while all three SApNPs outperformed the individual
333 S2GΔHR2 spike with a ranking of average EC₅₀ titers correlated with their size (FR < E2p < I3-
334 01v9). Sera reacted with the SARS-CoV-1 spike similarly, albeit at a lower level (**fig. S5A**).
335 Lastly, we compared the bAb responses induced by three SARS-CoV-1 vaccines, S2P_{ECTO} spike
336 (S2P_{ECTO}-5GS-1TD0), scaffolded RBD trimer (RBD-5GS-1TD0), and SPY-linked RBD SApNP
337 (RBD-5GS-SPY-5GS-FR) (**Fig. 4D** and **fig. S6**). Based on average EC₅₀ titers, the SARS-CoV-1

338 S2P_{ECTO} spike appeared to have elicited a more robust bAb response than the SARS-CoV-2
339 S2GΔHR2 spike, whereas the SARS-CoV-1 RBD SApNP was less advantageous than its SARS-
340 COV-2 counterpart. Serum reactivity with the SARS-CoV-2 S2P_{ECTO} spike was observed for all
341 three SARS-CoV-1 vaccine groups (**fig. S6A**). In summary, RBD SApNPs can elicit higher titers
342 of RBD-specific bAbs than the scaffolded RBD trimer and S2P_{ECTO} spike, albeit at different
343 levels for the two SARS-CoVs. The S2GΔHR2 spike is more immunogenic than the S2P_{ECTO}
344 spike, showing on average two-fold higher bAb titers. The S2GΔHR2-presenting E2p and I3-
345 01v9 SApNPs are the best performers among all the spike-based vaccines, consistent with our
346 previous findings for these two large SApNPs (57, 58, 60).

347 **SARS-CoV-1/2 vaccine-induced NAb response**

348 One major goal in COVID-19 vaccine development is to generate a potent NAb response that
349 can protect against SARS-CoV-2 infection. Pseudoparticle (SARS-CoV-1/2-pp) neutralization
350 assays (84) were used to evaluate serum NAb responses elicited by different vaccines. We first
351 analyzed the NAb responses, as measured by 50% inhibitory dilution (ID₅₀) titers, in the two
352 SARS-CoV-2 RBD vaccine groups (**Fig. 5A** and **fig. S7**). The SPY-linked RBD SApNP elicited
353 a NAb response against autologous SARS-CoV-2 as early as w2, albeit with low titers, and
354 retained its advantage at w5 and w8, suggesting that such RBD SApNP vaccines can elicit a
355 rapid NAb response. The scaffolded RBD trimer group showed higher average ID₅₀ titers than
356 the S2P_{ECTO} spike group at both w5 and w8. A somewhat different pattern was observed in the
357 SARS-CoV-1-pp assay. At w2, no vaccine group showed detectable heterologous NAb response.
358 At w5 and w8, the S2P_{ECTO} spike elicited a more potent anti-SARS-CoV-1 NAb response than
359 the scaffolded RBD trimer, suggesting that non-RBD epitopes on the spike may contribute to
360 cross-neutralization. We then analyzed the NAb responses induced by five spike-based vaccines

361 **(Fig. 5B and fig. S8)**. In terms of autologous neutralization, no spike-based vaccine elicited any
362 NAb response that blocks SARS-CoV-2-pps after one dose, but a consistent pattern of serum
363 neutralization was observed at w5 and w8 **(Fig. 5B, upper panel)**. Specifically, the S2P_{ECTO} spike
364 showed the lowest average ID₅₀ titers, 879 and 2481 at w5 and w8, respectively, whereas the
365 S2GΔHR2 spike induced a stronger NAb response with 2.8-6.7-fold higher average ID₅₀ titers,
366 which did not reach $P \leq 0.05$ due to within-group variation. Nonetheless, this result confirmed
367 the beneficial effect of the 2G mutation and the HR2 stalk deletion on NAb elicitation. Among
368 the three SApNPs, E2p was the best performer at w5, showing an average ID₅₀ titer of 8435 that
369 is 9.6-fold higher than S2P_{ECTO} and 1.4-fold higher than S2GΔHR2, while I3-01v9 showed the
370 most potent NAb response at w8 with an average ID₅₀ titer of 17351 that is about 7-fold and 2.5-
371 fold higher than S2P_{ECTO} and S2GΔHR2, respectively. A similar temporal pattern was observed
372 in the heterologous SARS-CoV-1-pp assay **(Fig. 5B, lower panel)**. It is worth noting that the
373 multilayered I3-01v9 SApNP elicited a SARS-CoV-1 NAb response with an average ID₅₀ titer of
374 351 at w2, whereas all other groups showed no detectable serum neutralization. These results
375 suggest that a well-designed SARS-CoV-2 S2GΔHR2 SApNP vaccine may provide protection
376 against both SARS-CoVs. Lastly, we analyzed the NAb responses induced by three SARS-CoV-
377 1 vaccines **(Fig. 5C and fig. S9)**. In the autologous SARS-CoV-1-pp assay, the S2P_{ECTO} spike
378 and the RBD SApNP induced significantly higher NAb titers than the scaffolded RBD trimer at
379 w2 and w5, and all three vaccine groups showed similar ID₅₀ titers at w8. However, heterologous
380 SARS-CoV-2 neutralization was below or at the baseline level for three SARS-CoV-1 vaccines
381 at w2, w5, and w8. In this study, the pseudovirus neutralization assay was validated using a panel
382 of known SARS-CoV-1/2 NAbs **(fig. S9C)**. As a negative control, the w8 mouse sera were tested
383 against pseudoparticles bearing the murine leukemia virus (MLV) Env, MLV-pps, showing no

384 detectable reactivity (**fig. S9D**). In summary, these results demonstrate an advantage in NAb
385 elicitation by the SARS-CoV-2 S2G Δ HR2 spike and its SApNPs compared to the widely used
386 S2P_{ECTO} spike. Although SARS-CoV-2 RBD- and S2G Δ HR2-presenting SApNPs are both
387 effective at eliciting an autologous NAb response, the latter can induce high NAb titers to SARS-
388 CoV-1 and may provide broader protection against SARS-associated CoVs.

389 **SARS-CoV-2 vaccine-induced T-cell response**

390 While humoral immunity is required to block host-virus interaction and prevent viral infection,
391 cellular immunity is essential for eliminating infected host cells to control viral infection (85-88).
392 Emerging evidence indicates that an early T-cell response (89, 90), as well as T-cell memory
393 (91), is critical for protection against SARS-CoV-2. However, COVID-19 vaccines must induce
394 a CD4⁺ T helper 1 (Th1), but not Th2-type, T-cell response, as the latter has been implicated in
395 vaccine-associated enhancement of respiratory disease (VAERD) (10). In addition, T follicular
396 helper cells (Tfh) play an important role in the maturation and production of NAb. Therefore,
397 understanding T-cell responses is crucial for development of an effective and safe COVID-19
398 vaccine.

399 Interferon (IFN)- γ -producing Th1 cells are important for generating an optimal antibody
400 response and for induction of cellular immunity (85-87). We first examined various SARS-CoV-
401 2 vaccines on induction of CD4⁺ Th1 responses specific to the vaccine antigen at w11, two
402 weeks after the fourth immunization, when memory T cells had already developed in spleen (88).
403 Mouse splenocytes from the S2P_{ECTO} group and two S2G Δ HR2 SApNP groups (E2p and I3-
404 01v9) were analyzed by flow cytometry using naïve samples as a negative control. The I3-01v9
405 group induced about 1.5- and 2.3-fold higher frequency of IFN- γ -producing CD4⁺ Th1 cells than

406 the S2P_{ECTO} and E2p groups, respectively (**Fig. 6A**). Notably, after re-stimulation with the
407 respective antigens for as few as 4 hours, both SApNP groups produced ~two-fold higher
408 frequency of CD107a-producing cytolytic CD4⁺ T cells than the S2P_{ECTO} and naïve groups (**Fig.**
409 **6B**). IFN- γ /IL-4 (interleukin-4) double-positive cells are memory CD4⁺ T cells that have
410 acquired the ability to produce IL-4 while still retaining the ability to produce IFN- γ under Th1
411 conditions (92). It appeared that I3-01v9 induced three- and five-fold more IFN- γ /IL-4 double-
412 positive memory CD4⁺ T cells than S2P_{ECTO} and E2p (**Fig. 6A**). These results suggest that I3-
413 01v9 can induce both CD4⁺ Th1 cells and IFN- γ /IL-4 double-positive memory CD4⁺ T cells. In
414 addition, I3-01v9 induced more IFN- γ /GM-CSF (granulocyte-macrophage colony-stimulating
415 factor) double-positive CD8⁺ effector T cells than S2P_{ECTO} and E2p (**Fig. 6C**), suggesting that
416 protective CD8⁺ T cells were also generated in mice immunized with I3-01v9. Of note, CD8⁺ T
417 cells derived from mice immunized with I3-01v9, rather than those with S2P_{ECTO} and E2p,
418 acquired the ability to rapidly produce IFN- γ upon antigen re-stimulation (**Fig. 6D**), suggesting
419 generation of I3-01v9-responsive effector/memory T cells. Our results indicate that the
420 S2G Δ HR2 I3-01v9 SApNP can induce robust T-cell responses consisting of CD4⁺ Th1 cells,
421 IFN- γ /IL-4 double-positive memory CD4⁺ T cells, and effector CD8⁺ T cells, thus providing
422 protective cellular immunity in addition to a potent NAb response. Since T cell immunity against
423 the SApNP backbone cannot be ruled out, a more detailed T-cell analysis using soluble spikes,
424 spike peptides, and naked SApNPs for re-stimulation may be warranted.

425 **DISCUSSION**

426 COVID-19 is the first worldwide pandemic of this scale since the infamous Spanish influenza
427 over a century ago (93), which caused ~50 million deaths worldwide and remains a painful
428 reminder of our vulnerability to a new virus without a protective vaccine. The rapid spread of

429 SARS-CoV-2 therefore demanded rapid vaccine development (10). Operation Warp Speed
430 (OWS) was launched in May 2020 with the initial goal to deliver 300 million doses of safe and
431 effective vaccines by January 2021 (94), although that goal has not yet been realized.
432 Nevertheless, in December 2020, while other vaccine candidates were still being evaluated in
433 clinical trials, two OWS-supported mRNA vaccines were approved for EUA, marking an
434 important turning point in the battle against the pandemic. However, vaccine development during
435 a pandemic against a new virus poses unique challenges, one of which is how to balance public
436 health needs versus scientific rigor (95-97). The global vaccine campaign also provides a unique
437 opportunity to compare different vaccine design strategies and platforms – especially new ones –
438 against a common target. While mRNA and viral vector vaccines remain the front runners,
439 protein-based vaccines are highlighted in a recent review with the prediction that they will
440 eventually reach a larger fraction of the global population (98). As the NAb titers induced by the
441 first-generation nucleic acid vaccines wane over time, effective protein vaccines will be needed
442 to sustain long-term immunity against SARS-CoV-2.

443 Here, we approached SARS-CoV-2 vaccine with a rational design strategy and set out to
444 develop protein nanoparticle vaccines that can be used alone or as a booster vaccine. To this end,
445 a panel of vaccine candidates have been generated based on three SApNP platforms with
446 different *in vitro* and *in vivo* attributes (**table S1**). Our comparative analysis of these vaccine
447 constructs has offered some valuable insights. First, the choice of antigen is critical to the
448 success of SARS-CoV-2 vaccine irrespective of the delivery platform. Most vaccine antigens
449 including OWS's vaccine candidates are based on S2P, which produces a spike structure that
450 differs in detail from the full-length wildtype spike, e.g. in FPPR of S2 and in the relative
451 dispositions of the S1 domains (52). These differences may complicate interpretation of vaccine

452 outcome. S2P and other empirical spike designs (53) have attempted to constrain the spike
453 conformation and increase trimer yield. However, as we previously demonstrated for HIV-1 Env
454 and EBOV GP (58, 60, 81), it is important to identify and eliminate (if possible) the cause of
455 spike metastability. During antigen screening, we found that deletion of the HR2 stalk with a 2P-
456 to-2G substitution renders a more stable spike, which is consistent with recent reports on a highly
457 flexible HR2 stalk in the native spikes on SARS-CoV-2 virions (54-56). Thus, S2GΔHR2 would
458 seem to represent a major advance in spike design. Second, single-component SApNPs provide a
459 powerful platform for vaccine development against diverse viral pathogens (57, 58, 60). Here,
460 S2GΔHR2 was genetically fused, rather than chemically linked, to three SApNPs, including two
461 multilayered 60-meric carriers with enhanced stability and an embedded T-help signal. Such
462 protein vaccines should be more effective in eliciting a potent NAb response and less likely to
463 induce adverse responses (98, 99). An epitope-focused vaccine strategy was also explored by
464 designing scaffolded RBD trimers and SPY-linked RBD SApNPs. Third, to achieve high
465 efficacy and ensure safety, vaccine-induced NAb and T-cell responses must be evaluated in
466 animals prior to clinical trials. Indeed, in our mouse study, S2GΔHR2 appeared to be more
467 effective than S2P in NAb elicitation, both alone and displayed on SApNPs. Of note, the
468 multilayered S2GΔHR2 I3-01v9 SApNP elicited not only high NAb titers but also desired T-cell
469 responses. In addition to CD4⁺ Th1 cells and memory CD4⁺ T cells, this SApNP also induced
470 CD107a-producing cytolytic CD4⁺ T cells, which may directly kill infected host cells, and GM-
471 CSF-producing CD8⁺ effector T cells, which may promote the generation of macrophages and
472 functional dendritic cells (DCs) to facilitate the clearance of infected cells. It is also worth noting
473 that the NAb response to the large SApNPs plateaued after three doses, suggesting that the
474 number of injections and dosage can be reduced without diminishing vaccine-induced responses.

475 Lastly, expression of vaccine antigens in CHO cells followed by purification using an antibody
476 column, such as CR3022, would allow rapid and industrial-scale vaccine production. In
477 summary, our study provides promising COVID-19 vaccine candidates for evaluation in clinical
478 trials.

479 **MATERIALS AND METHODS**

480 **Design, expression, and purification of SARS-CoV-1/2 RBD and spike antigens**

481 The spike (S) genes of the SARS-CoV-1 isolate Tor2 (GenBank accession #: NC_004718) and
482 the SARS-CoV-2 isolate Wuhan-Hu-1 (GenBank accession #: MN908947) were used to design
483 all the RBD and spike constructs following codon-optimization for expression in mammalian
484 cells. The RBD sequence is defined as P317-D518 and P330-N532 for SARS-CoV-1 and 2,
485 respectively. The S_{ECTO} sequence is defined as M1-Q1190 and M1-Q1208 for SARS-CoV-1 and
486 2, respectively. To remove the S1/S2 cleavage site, an R667G mutation and a ⁶⁸²GSAGSV⁶⁸⁷
487 modification were introduced in the SARS-CoV-1 and 2 spikes, respectively. The 2P (or 2G)
488 mutation was made to K968/V969 and K986/V987 in the SARS-CoV-1 and 2 spikes,
489 respectively. The SARS-CoV-2 C-terminal region (E1150-Q1208) containing the HR2 stalk was
490 removed from S2G_{ECTO}, resulting in an HR2-deleted spike construct, termed S2G Δ HR2. The
491 viral capsid protein SHP (PDB: 1TD0) was used as a trimerization motif in spike constructs for
492 immunization, whereas the foldon domain from the bacteriophage T4 fibrin (PDB: 1RFO) was
493 used in coating spike antigens for ELISA to mask the 1TD0-derived antibody response. All
494 constructs were transiently expressed in ExpiCHO cells (Thermo Fisher). Briefly, ExpiCHO
495 cells were thawed and incubated with ExpiCHOTM Expression Medium (Thermo Fisher) in a
496 shaker incubator at 37 °C, 135 rpm and 8% CO₂. When the cells reached a density of 10 \times 10⁶ ml⁻¹
497 ¹, ExpiCHOTM Expression Medium was added to reduce cell density to 6 \times 10⁶ ml⁻¹ for

498 transfection. The ExpiFectamineTM CHO/plasmid DNA complexes were prepared for 100-ml
499 transfection in ExpiCHO cells following the manufacturer's instructions. For a given construct,
500 100 µg of plasmid and 320 µl of ExpiFectamineTM CHO reagent were mixed in 7.7 ml of cold
501 OptiPROTM medium (Thermo Fisher). After the first feed on day one, ExpiCHO cells were
502 cultured in a shaker incubator at 33 °C, 115 rpm and 8% CO₂ following the Max Titer protocol
503 with an additional feed on day five (Thermo Fisher). Culture supernatants were harvested 13 to
504 14 days after transfection, clarified by centrifugation at 4000 rpm for 25 min, and filtered using a
505 0.45 µm filter (Thermo Fisher). The CR3022 antibody column was used to extract SARS-CoV-
506 1/2 antigens from the supernatants, which was followed by SEC on a Superdex 200 10/300 GL
507 column (for scaffolded RBD trimers) or a Superose 6 10/300 GL column (for SPY-linked RBD
508 SApNPs, spikes, and S2GΔHR2 SApNPs). A human NAb, P2B-2F6 (36), was also used to pack
509 antibody columns for purification of the SARS-CoV-2 S2GΔHR2 spike, which was followed by
510 SEC on a HiLoad 16/600 Superose 6 column. For comparison, His₆-tagged S_{ECTO}-5GS-1TD0
511 spike protein was extracted from the supernatants using an immobilized Ni SepharoseTM Excel
512 column (GE Healthcare) and eluted with 500 mM Imidazole prior to SEC. Protein concentration
513 was determined using UV₂₈₀ absorbance with theoretical extinction coefficients.

514 **Blue native polyacrylamide gel electrophoresis**

515 SARS-CoV-2 spikes and spike-presenting SApNPs were analyzed by blue native polyacrylamide
516 gel electrophoresis (*BN-PAGE*) and stained with Coomassie blue. The proteins were mixed with
517 sample buffer and G250 loading dye and added to a 4-12% Bis-Tris NativePAGETM gel (Life
518 Technologies). BN-PAGE gels were run for 2 to 2.5 hours at 150 V using the NativePAGETM
519 running buffer (Life Technologies) according to the manufacturer's instructions.

520 **Enzyme-linked immunosorbent assay**

521 Each well of a CostarTM 96-well assay plate (Corning) was first coated with 50 μ l PBS
522 containing 0.2 μ g of the appropriate antigens. The plates were incubated overnight at 4 °C, and
523 then washed five times with wash buffer containing PBS and 0.05% (v/v) Tween 20. Each well
524 was then coated with 150 μ l of a blocking buffer consisting of PBS and 40 mg ml⁻¹ blotting-
525 grade blocker (Bio-Rad). The plates were incubated with the blocking buffer for 1 hour at room
526 temperature, and then washed five times with wash buffer. For antigen binding, antibodies (in
527 the immunoglobulin G (IgG) form) were diluted in the blocking buffer to a maximum
528 concentration of 5 μ g ml⁻¹ followed by a 10-fold dilution series. For each antibody dilution, a
529 total of 50 μ l volume was added to the appropriate wells. For mouse sample analysis, plasma
530 was diluted by 20-fold in the blocking buffer and subjected to a 10-fold dilution series. For each
531 sample dilution, a total of 50 μ l volume was added to the wells. Each plate was incubated for 1
532 hour at room temperature, and then washed 5 times with PBS containing 0.05% Tween 20. For
533 antibody binding, a 1:5000 dilution of goat anti-human IgG antibody (Jackson ImmunoResearch
534 Laboratories, Inc), or for mouse sample analysis, a 1:3000 dilution of horseradish peroxidase
535 (HRP)-labeled goat anti-mouse IgG antibody (Jackson ImmunoResearch Laboratories), was then
536 made in the wash buffer (PBS containing 0.05% Tween 20), with 50 μ l of this diluted secondary
537 antibody added to each well. The plates were incubated with the secondary antibody for 1 hour at
538 room temperature, and then washed 6 times with PBS containing 0.05% Tween 20. Finally, the
539 wells were developed with 50 μ l of TMB (Life Sciences) for 3-5 min before stopping the
540 reaction with 50 μ l of 2 N sulfuric acid. The resulting plate readouts were measured at a
541 wavelength of 450 nm. Of note, the w2 serum binding did not reach the plateau (or saturation) to
542 allow for accurate determination of EC₅₀ titers. Nonetheless, the EC₅₀ values at w2 were derived

543 by setting the lower/upper constraints of OD₄₅₀ at 0.0/3.2 to facilitate the comparison of different
544 vaccine groups at the first time point.

545 **Bio-layer interferometry**

546 The kinetics of SARS-CoV-1/2 vaccine antigens, RBD versus RBD-presenting SApNPs as well
547 as spike versus spike-presenting SApNPs, binding to a panel of known antibodies (in the IgG
548 form) was measured using an Octet RED96 instrument (FortéBio, Pall Life Sciences). All assays
549 were performed with agitation set to 1000 rpm in FortéBio 1× kinetic buffer. The final volume
550 for all the solutions was 200 µl per well. Assays were performed at 30 °C in solid black 96-well
551 plates (Geiger Bio-One). For all antigens except for S2GΔHR2 SApNPs, 5 µg ml⁻¹ of antibody in
552 1× kinetic buffer was loaded onto the surface of anti-human Fc Capture Biosensors (AHC) for
553 300 s. For S2GΔHR2 SApNPs, anti-human Fc Quantitation Biosensors (AHQ) were used. A 60 s
554 biosensor baseline step was applied prior to the analysis of the association of the antibody on the
555 biosensor to the antigen in solution for 200 s. A two-fold concentration gradient of antigen,
556 starting at 950 nM for scaffolded RBD trimers, 37 nM for SPY-linked RBD FR SApNP (RBD-
557 5GS-SPY-5GS-FR), 150 nM for soluble spikes, and 9/3.5/3.5 nM for S2GΔHR2 presented on
558 FR/E2p/I3-01v9 SApNPs, was used in a titration series of six. The dissociation of the interaction
559 was followed for 300 s. Correction of baseline drift was performed by subtracting the mean value
560 of shifts recorded for a sensor loaded with antibody but not incubated with antigen, and for a
561 sensor without antibody but incubated with antigen. Octet data were processed by FortéBio's
562 data acquisition software v.8.1. Experimental data were fitted with the binding equations
563 describing a 2:1 interaction to achieve optimal fitting. Of note, the S2GΔHR2 spike was also
564 measured using AHQ biosensors to facilitate comparison of mAb binding with the S2GΔHR2-
565 presenting SApNPs.

566 **Differential scanning calorimetry (DSC)**

567 Thermal melting curves of SARS-CoV-2 S2_{PECTO}-5GS-1TD0 and S2GΔHR2-5GS-1TD0 spike
568 proteins following CR3022 and SEC purification were obtained from a MicroCal PEAQ-DSC
569 Man instrument (Malvern). The purified spike trimer protein produced from ExpiCHO cells were
570 buffer exchanged into 1×PBS and concentrated to 0.8 μM before analysis by the instrument.
571 Melting was probed at a scan rate of 60 °C·h⁻¹ from 20 °C to 100 °C. Data processing, including
572 buffer correction, normalization, and baseline subtraction, was conducted using the MicroCal
573 PEAQ-DSC software. Gaussian fitting was performed using the Origin 9.0 software.

574 **Electron microscopy (EM) assessment of nanoparticle constructs**

575 The EM analysis of various RBD and S2GΔHR2-presenting SApNPs was performed by the Core
576 Microscopy Facility at The Scripps Research Institute. All SApNP samples were prepared at the
577 concentration of 0.01-0.05 mg/ml. Carbon-coated copper grids (400 mesh) were glow-discharged
578 and 8 μL of each sample was adsorbed for 2 min. Excess sample was wicked away and grids
579 were negatively stained with 2% uranyl formate for 2 min. Excess stain was wicked away and
580 the grids were allowed to dry. Samples were analyzed at 80 kV with a Talos L120C transmission
581 electron microscope (Thermo Fisher) and images were acquired with a CETA 16M CMOS
582 camera.

583 **Animal immunization and sample collection**

584 Similar immunization protocols have been reported in our previous vaccine studies (57, 58, 60).
585 Briefly, the Institutional Animal Care and Use Committee (IACUC) guidelines were followed
586 with animal subjects tested in the immunization study. Eight-week-old BALB/c mice were
587 purchased from The Jackson Laboratory and housed in ventilated cages in environmentally

588 controlled rooms at The Scripps Research Institute, in compliance with an approved IACUC
589 protocol and AAALAC (Association for Assessment and Accreditation of Laboratory Animal
590 Care) International guidelines. Mice were immunized at weeks 0, 3, 6, and 9 with 200 μ l of
591 antigen/adjuvant mix containing 50 μ g of vaccine antigen and 100 μ l of adjuvant, AddaVax or
592 Adju-Phos (InvivoGen), via the intraperitoneal (i.p.) route. Blood was collected two weeks after
593 each immunization. All bleeds were performed through the retro-orbital sinus using heparinized
594 capillary tubes into EDTA-coated tubes. Samples were spun at 1200 RPM for 10 min to separate
595 plasma (top layer) and the rest of the whole blood layer. Upon heat inactivation at 56 °C for 30
596 min, the plasma was spun at 2000 RPM for 10 min to remove precipitates. The rest of the whole
597 blood layer was diluted with an equal volume of PBS and then overlaid on 4.5 ml of Ficoll in a
598 15 ml SepMate™ tube (STEMCELL Technologies) and spun at 1200 RPM for 10 min at 20 °C
599 to separate peripheral blood mononuclear cells (PBMCs). Cells were washed once in PBS and
600 then resuspended in 1 ml of ACK Red Blood Cell lysis buffer (Lonza). After washing with PBS,
601 PBMCs were resuspended in 2 ml of Bambanker Freezing Media (Lymphotec). Spleens were
602 harvested at w11 and ground against a 70- μ m cell strainer (BD Falcon) to release the splenocytes
603 into a cell suspension. Splenocytes were centrifuged, washed in PBS, treated with 5 ml of ACK
604 lysing buffer (Lonza), and frozen with 3ml of Bambanker freezing media. Plasma was used for
605 ELISA and neutralization assays to determine binding and neutralizing antibody responses in
606 mouse serum.

607 **SARS-CoV-1/2 pseudovirus neutralization assay**

608 Pseudoparticle (SARS-CoV-1/2-pp) neutralization assays were utilized to assess the neutralizing
609 activity of previously reported antibodies and vaccine-induced murine antibody response. SARS-
610 CoV-1/2-pps were generated by co-transfection of HEK293T cells with the HIV-1 pNL4-3.lucR-

611 E- plasmid (obtained from the NIH AIDS reagent program: <https://www.aidsreagent.org/>) and
612 the expression plasmid encoding the S gene of SARS-CoV-1 isolate Tor2 (GenBank accession #:
613 NC_004718) and the SARS-CoV-2 isolate Wuhan-Hu-1 (GenBank accession #: MN908947) at a
614 4:1 ratio by lipofectamine 3000 (Thermo Fisher Scientific). After 48 to 72 hours, SARS-CoV-
615 1/2-pps were collected from the supernatant by centrifugation at 4000 rpm for 10 min, aliquoted,
616 and stored at -80 °C before use. The mAbs at a starting concentration of 0.1-10 µg/ml, or mouse
617 plasma at a starting dilution of 100-fold, were mixed with the supernatant containing SARS-
618 CoV-1/2-pps and incubated for 1 hour at 37°C in white solid-bottom 96-well plate (Corning). A
619 3-fold dilution series was used in the assay. The HEK293T-hACE2 cell line (catalogue#: NR-
620 52511) and the vector pcDNA3.1(-) containing the SARS-CoV-2 S gene (catalogue#: NR52420)
621 were obtained from BEI RESOURCES (<https://www.beiresources.org/>) and used in pseudovirus
622 neutralization assays (84). Briefly, HEK293T-hACE2 cells at 1×10^4 were added to each well and
623 the plate was incubated at 37°C for 48 hours. After incubation, overlying media was removed,
624 and cells were lysed. The firefly luciferase signal from infected cells was determined using the
625 Bright-Glo Luciferase Assay System (Promega) according to the manufacturer's instructions.
626 Data were retrieved from a BioTek microplate reader with Gen 5 software, the average
627 background luminescence from a series of uninfected wells was subtracted from each well, and
628 neutralization curves were generated using GraphPad Prism 8.4.3, in which values from wells
629 were compared against a well containing SARS-CoV-1/2-pp only. The same HIV-1 vectors
630 pseudotyped with the murine leukemia virus (MLV) Env gene, termed MLV-pps, were produced
631 in HEK293T cells and included in the neutralization assays as a negative control. As the NAb
632 titers plateaued after w8, the w11 results were not shown in Fig. 5 but included in figs. S7-S9 for
633 comparison.

634 **Dendritic cell (DC) production**

635 Mouse bone marrow (BM) was cultured in RPMI 1640 medium containing 10% fetal bovine
636 serum and recombinant mouse Flt3L (50 ng/mL) and SCF (10 ng/ml) for 9 days as described
637 (100). To induce DC activation, immature DCs were incubated with lipopolysaccharide (LPS,
638 100 ng/mL), R848 (Resiquimod, 100 ng/mL) or CpG (ODN 1585, 1 μ M) overnight, which
639 activated Toll-like receptor (TLR)4 , TLR7/8 or TLR9 signaling, respectively. Cells were
640 harvested for experiments. pDCs were sorted to isolate CD11c⁺B220⁺ cells using FACS cell
641 sorter and magnetic beads (Miltenyi-Biotech, CA).

642 **Antibodies and flow cytometry analysis**

643 All antibodies used for immunofluorescence staining were purchased from eBioscience (San
644 Diego, CA), BioLegend (San Diego, CA) or BD Biosciences (San Jose, CA). Magnetic
645 microbead-conjugated Abs and streptavidin were purchased from Miltenyi-Biotech (Auburn,
646 CA). Recombinant human IL-2 protein was purchased from R&D Systems (Minneapolis, MN).
647 Recombinant mouse Flt3 ligand (Flt3L) and mouse SCF were purchased from Shenandoah
648 Biotech (Warwick, PA). Cells were stained with appropriate concentrations of mAbs. Dead cells
649 were excluded using Fixable Viability Dye from eBioscience (San Diego, CA). Flow cytometry
650 (FC) analyses were performed using LSRII (BD Bioscience, CA) and Canto cytometers (Becton
651 Dickinson, NJ). Cells were sorted on BD FACSAria II (BD Bioscience, CA).

652 **T cell culture and activation**

653 Splenic mononuclear cells from each group of immunized mice were cultured in the presence of
654 DCs pulsed with or without S2P_{ECTO}, multilayered S2G Δ HR2-presenting E2P or I3-01v9 SApNP

655 $(1 \times 10^{-7} \mu\text{M})$ in complete IMDM medium containing IL-2 (5.0 ng/ml). Cells were collected 16
656 hours and 4 hours later for intracellular cytokine staining and flow cytometric analysis.

657 **Statistics**

658 In antibody analysis, comparison of different vaccine groups was performed in GraphPad Prism
659 8.4.3 using the two-tailed unpaired Student's *t* test. In T cell analysis, comparison of means was
660 done using the two-tailed unpaired Student's *t* test, ANOVA and then post-hoc *t* test. P values of
661 0.05 or less were considered significant.

662

663 **SUPPLEMENTARY MATERIALS**

664 Supplementary material for this article is available at <http://xxx/xxx/xxx>.

665 **fig. S1.** In-vitro characterization of SARS-CoV-1/2 RBD-based immunogens.

666 **fig. S2.** In-vitro characterization of SARS-CoV-2 spike antigens.

667 **fig. S3.** In-vitro characterization of SARS-CoV-2 S2GΔHR2 SApNPs.

668 **fig. S4.** SARS-CoV-2 RBD/RBD-SApNP vaccine-induced binding antibody responses.

669 **fig. S5.** SARS-CoV-2 spike/spike-SApNP vaccine-induced binding antibody responses.

670 **fig. S6.** SARS-CoV-1 spike/RBD/RBD-SApNP vaccine-induced binding antibody responses.

671 **fig. S7.** SARS-CoV-2 RBD/RBD-SApNP vaccine-induced neutralizing antibody responses.

672 **fig. S8.** SARS-CoV-2 spike/spike-SApNP vaccine-induced neutralizing antibody responses.

673 **fig. S9.** SARS-CoV-1 spike/RBD/RBD-SApNP vaccine-induced neutralizing antibody
674 responses.

675 **table. S1.** Key *in vitro* and *in vivo* characteristics of RBD and spike-based SARS-CoV-2
676 vaccines.

677

References

- 678
679 1. N. Zhu *et al.*, A novel coronavirus from patients with pneumonia in China, 2019. *N. Engl.*
680 *J. Med.* **382**, 727-733 (2020).
681 2. P. Zhou *et al.*, A pneumonia outbreak associated with a new coronavirus of probable bat
682 origin. *Nature* **579**, 270-273 (2020).
683 3. F. Wu *et al.*, A new coronavirus associated with human respiratory disease in China.
684 *Nature* **579**, 265-226 (2020).
685 4. E. S. Dong, H. R. Du, L. Gardner, An interactive web-based dashboard to track COVID-
686 19 in real time. *Lancet Infect. Dis.* **20**, 533-534 (2020).
687 5. M. Hoffmann *et al.*, SARS-CoV-2 cell entry depends on ACE2 and TMPRSS2 and is
688 blocked by a clinically proven protease inhibitor. *Cell* **181**, 271-280.e278 (2020).
689 6. M. Z. Tay, C. M. Poh, L. Renia, P. A. MacAry, L. F. P. Ng, The trinity of COVID-19:
690 immunity, inflammation and intervention. *Nat. Rev. Immunol.* **20**, 363-374 (2020).
691 7. T. Zohar, G. Alter, Dissecting antibody-mediated protection against SARS-CoV-2. *Nat.*
692 *Rev. Immunol.* **20**, 392-394 (2020).
693 8. N. Vabret *et al.*, Immunology of COVID-19: Current state of the science. *Immunity* **52**,
694 910-941 (2020).
695 9. N. Lurie, M. Saville, R. Hatchett, J. Halton, Developing Covid-19 vaccines at pandemic
696 speed. *N. Engl. J. Med.* **382**, 1969-1973 (2020).
697 10. B. S. Graham, Rapid COVID-19 vaccine development. *Science* **368**, 945-946 (2020).
698 11. F. Krammer, SARS-CoV-2 vaccines in development. *Nature* **586**, 516-527 (2020).
699 12. T. T. Le, J. P. Cramer, R. Chen, S. Mayhew, Evolution of the COVID-19 vaccine
700 development landscape. *Nat. Rev. Drug Discov.* **19**, 667-668 (2020).
701 13. Q. Gao *et al.*, Development of an inactivated vaccine candidate for SARS-CoV-2.
702 *Science* **369**, 77-81 (2020).
703 14. H. Wang *et al.*, Development of an inactivated vaccine candidate, BBIBP-CorV, with
704 potent protection against SARS-CoV-2. *Cell* **182**, 713-721.e719 (2020).
705 15. N. van Doremalen *et al.*, ChAdOx1 nCoV-19 vaccine prevents SARS-CoV-2 pneumonia
706 in rhesus macaques. *Nature* **586**, 578-582 (2020).
707 16. P. M. Folegatti *et al.*, Safety and immunogenicity of the ChAdOx1 nCoV-19 vaccine
708 against SARS-CoV-2: a preliminary report of a phase 1/2, single-blind, randomised
709 controlled trial. *Lancet* **396**, 467-478 (2020).
710 17. N. B. Mercado *et al.*, Single-shot Ad26 vaccine protects against SARS-CoV-2 in rhesus
711 macaques. *Nature* **586**, 583-588 (2020).
712 18. F.-C. Zhu *et al.*, Safety, tolerability, and immunogenicity of a recombinant adenovirus
713 type-5 vectored COVID-19 vaccine: a dose-escalation, open-label, non-randomised, first-
714 in-human trial. *Lancet* **395**, 1845-1854 (2020).
715 19. T. R. F. Smith *et al.*, Immunogenicity of a DNA vaccine candidate for COVID-19. *Nat.*
716 *Commun.* **11**, 2601 (2020).
717 20. J. Yu *et al.*, DNA vaccine protection against SARS-CoV-2 in rhesus macaques. *Science*
718 **369**, 806-811 (2020).
719 21. A. Patel *et al.*, Intradermal-delivered DNA vaccine provides anamnestic protection in a
720 rhesus macaque SARS-CoV-2 challenge model. *bioRxiv*, 2020.2007.2028.225649 (2020).
721 22. L. A. Jackson *et al.*, An mRNA vaccine against SARS-CoV-2 - preliminary report. *N.*
722 *Engl. J. Med.* **383**, 1920-1931 (2020).

- 723 23. E. E. Walsh *et al.*, Safety and immunogenicity of two RNA-based Covid-19 vaccine
724 candidates. *N. Engl. J. Med.* **383**, 2439-2450 (2020).
- 725 24. J.-H. Tian *et al.*, SARS-CoV-2 spike glycoprotein vaccine candidate NVX-CoV2373
726 elicits immunogenicity in baboons and protection in mice. *bioRxiv*,
727 2020.2006.2029.178509 (2020).
- 728 25. C. Keech *et al.*, Phase 1-2 trial of a SARS-CoV-2 recombinant spike protein nanoparticle
729 vaccine. *N. Engl. J. Med.* **383**, 2320-2332 (2020).
- 730 26. M. Voysey *et al.*, Safety and efficacy of the ChAdOx1 nCoV-19 vaccine (AZD1222)
731 against SARS-CoV-2: an interim analysis of four randomised controlled trials in Brazil,
732 South Africa, and the UK. *Lancet*, Online ahead of print (2020).
- 733 27. F. P. Polack *et al.*, Safety and efficacy of the BNT162b2 mRNA Covid-19 vaccine. *N.*
734 *Engl. J. Med.*, Online ahead of print (2020).
- 735 28. L. R. Baden *et al.*, Efficacy and safety of the mRNA-1273 SARS-CoV-2 vaccine. *N.*
736 *Engl. J. Med.*, Online ahead of print (2020).
- 737 29. J. Shang *et al.*, Cell entry mechanisms of SARS-CoV-2. *Proc. Natl. Acad. Sci. U. S. A.*
738 **117**, 11727-11734 (2020).
- 739 30. L. Y. Du *et al.*, The spike protein of SARS-CoV - a target for vaccine and therapeutic
740 development. *Nat. Rev. Microbiol.* **7**, 226-236 (2009).
- 741 31. K. Duan *et al.*, Effectiveness of convalescent plasma therapy in severe COVID-19
742 patients. *Proc. Natl. Acad. Sci. U. S. A.* **117**, 9490-9496 (2020).
- 743 32. S. B. Jiang, C. Hillyer, L. Y. Du, Neutralizing antibodies against SARS-CoV-2 and other
744 human coronaviruses. *Trends Immunol.* **41**, 355-359 (2020).
- 745 33. D. Pinto *et al.*, Cross-neutralization of SARS-CoV-2 by a human monoclonal SARS-CoV
746 antibody. *Nature* **583**, 290-295.
- 747 34. X. Tian *et al.*, Potent binding of 2019 novel coronavirus spike protein by a SARS
748 coronavirus-specific human monoclonal antibody. *Emerg. Microbes Infect.* **9**, 382-385
749 (2020).
- 750 35. S. J. Zost *et al.*, Rapid isolation and profiling of a diverse panel of human monoclonal
751 antibodies targeting the SARS-CoV-2 spike protein. *Nat. Med.* **26**, 1422-1427.
- 752 36. B. Ju *et al.*, Human neutralizing antibodies elicited by SARS-CoV-2 infection. *Nature*
753 **584**, 115-119 (2020).
- 754 37. R. Shi *et al.*, A human neutralizing antibody targets the receptor-binding site of SARS-
755 CoV-2. *Nature* **584**, 120-124 (2020).
- 756 38. Y. Wu *et al.*, A noncompeting pair of human neutralizing antibodies block COVID-19
757 virus binding to its receptor ACE2. *Science* **368**, 1274-1278 (2020).
- 758 39. Y. L. Cao *et al.*, Potent neutralizing antibodies against SARS-CoV-2 identified by high-
759 throughput single-cell sequencing of convalescent patients' B cells. *Cell* **182**, 73-84.e16
760 (2020).
- 761 40. D. F. Robbiani *et al.*, Convergent antibody responses to SARS-CoV-2 in convalescent
762 individuals. *Nature* **584**, 437-442 (2020).
- 763 41. T. F. Rogers *et al.*, Isolation of potent SARS-CoV-2 neutralizing antibodies and
764 protection from disease in a small animal model. *Science* **369**, 956-963 (2020).
- 765 42. J. D. Huo *et al.*, Neutralizing nanobodies bind SARS-CoV-2 spike RBD and block
766 interaction with ACE2. *Nat. Struct. Mol. Biol.* **27**, 846-854.
- 767 43. D. Wrapp *et al.*, Structural basis for potent neutralization of betacoronaviruses by single-
768 domain camelid antibodies. *Cell* **181**, 1004-1015.e1015 (2020).

- 769 44. D. Wrapp *et al.*, Cryo-EM structure of the 2019-nCoV spike in the prefusion
770 conformation. *Science* **367**, 1260-1263 (2020).
- 771 45. A. C. Walls *et al.*, Structure, function, and antigenicity of the SARS-CoV-2 spike
772 glycoprotein. *Cell* **181**, 281-292.e286 (2020).
- 773 46. R. Yan *et al.*, Structural basis for the recognition of SARS-CoV-2 by full-length human
774 ACE2. *Science* **367**, 1444-1448 (2020).
- 775 47. J. Shang *et al.*, Structural basis of receptor recognition by SARS-CoV-2. *Nature* **581**,
776 221-224 (2020).
- 777 48. T. Zhou *et al.*, Cryo-EM structures of SARS-CoV-2 spike without and with ACE2 reveal
778 a pH-dependent switch to mediate endosomal positioning of receptor-binding domains.
779 *Cell Host Microbe* **28**, 867-879.e865 (2020).
- 780 49. C. O. Barnes *et al.*, Structures of human antibodies bound to SARS-CoV-2 spike reveal
781 common epitopes and recurrent features of antibodies. *Cell* **82**, 828-842.e816 (2020).
- 782 50. M. Yuan *et al.*, A highly conserved cryptic epitope in the receptor binding domains of
783 SARS-CoV-2 and SARS-CoV. *Science* **368**, 630-633 (2020).
- 784 51. M. Yuan *et al.*, Structural basis of a shared antibody response to SARS-CoV-2. *Science*
785 **369**, 1119-1123 (2020).
- 786 52. Y. Cai *et al.*, Distinct conformational states of SARS-CoV-2 spike protein. *Science* **369**,
787 1586-1592 (2020).
- 788 53. C.-L. Hsieh *et al.*, Structure-based design of prefusion-stabilized SARS-CoV-2 spikes.
789 *Science* **369**, 1501-1505 (2020).
- 790 54. H. Yao *et al.*, Molecular architecture of the SARS-CoV-2 virus. *Cell* **183**, 730-738.e713
791 (2020).
- 792 55. Z. Ke *et al.*, Structures and distributions of SARS-CoV-2 spike proteins on intact virions.
793 *Nature* **588**, 498-502 (2020).
- 794 56. B. Turonova *et al.*, In situ structural analysis of SARS-CoV-2 spike reveals flexibility
795 mediated by three hinges. *Science* **370**, 203-208 (2020).
- 796 57. L. L. He *et al.*, Proof of concept for rational design of hepatitis C virus E2 core
797 nanoparticle vaccines. *Sci. Adv.* **6**, eaaz6225 (2020).
- 798 58. L. He *et al.*, HIV-1 vaccine design through minimizing envelope metastability. *Sci. Adv.*
799 **4**, aau6769 (2018).
- 800 59. L. He *et al.*, Presenting native-like trimeric HIV-1 antigens with self-assembling
801 nanoparticles. *Nat. Commun.* **7**, 12041 (2016).
- 802 60. L. He *et al.*, Single-component multilayered self-assembling nanoparticles presenting
803 rationally designed glycoprotein trimers as Ebola virus vaccines. *bioRxiv*,
804 2020.2008.2022.262634 (2020).
- 805 61. B. Zakeri *et al.*, Peptide tag forming a rapid covalent bond to a protein, through
806 engineering a bacterial adhesin. *Proc. Natl. Acad. Sci. U. S. A.* **109**, E690-E697 (2012).
- 807 62. J. Lan *et al.*, Structure of the SARS-CoV-2 spike receptor-binding domain bound to the
808 ACE2 receptor. *Nature* **581**, 215-220 (2020).
- 809 63. R. N. Kirchdoerfer *et al.*, Stabilized coronavirus spikes are resistant to conformational
810 changes induced by receptor recognition or proteolysis. *Sci. Rep.* **8**, 15701 (2018).
- 811 64. Y. Yuan *et al.*, Cryo-EM structures of MERS-CoV and SARS-CoV spike glycoproteins
812 reveal the dynamic receptor binding domains. *Nat. Commun.* **8**, 15092 (2017).

- 813 65. R. W. Sanders *et al.*, A next-generation cleaved, soluble HIV-1 Env trimer, BG505
814 SOSIP.664 gp140, expresses multiple epitopes for broadly neutralizing but not non-
815 neutralizing antibodies. *PLoS Pathog.* **9**, e1003618 (2013).
- 816 66. P. Pugach *et al.*, A native-like SOSIP.664 trimer based on an HIV-1 subtype B env gene.
817 *J. Virol.* **89**, 3380-3395 (2015).
- 818 67. J. ter Meulen *et al.*, Human monoclonal antibody combination against SARS coronavirus:
819 Synergy and coverage of escape mutants. *PLoS Med.* **3**, 1071-1079 (2006).
- 820 68. P. Prabakaran *et al.*, Structure of severe acute respiratory syndrome coronavirus receptor-
821 binding domain complexed with neutralizing antibody. *J. Biol. Chem.* **281**, 15829-15836
822 (2006).
- 823 69. W. C. Hwang *et al.*, Structural basis of neutralization by a human anti-severe acute
824 respiratory syndrome spike protein antibody, 80R. *J. Biol. Chem.* **281**, 34610-34616
825 (2006).
- 826 70. A. C. Walls *et al.*, Unexpected receptor functional mimicry elucidates activation of
827 coronavirus fusion. *Cell* **176**, 1026-1039.e1015 (2019).
- 828 71. T. U. J. Bruun, A. M. C. Andersson, S. J. Draper, M. Howarth, Engineering a rugged
829 nanoscaffold to enhance plug-and-display vaccination. *Acs Nano* **12**, 8855-8866 (2018).
- 830 72. L. Chu, D. K. Robinson, Industrial choices for protein production by large-scale cell
831 culture. *Curr. Opin. Biotechnol.* **12**, 180-187 (2001).
- 832 73. Y. Durocher, M. Butler, Expression systems for therapeutic glycoprotein production.
833 *Curr. Opin. Biotechnol.* **20**, 700-707 (2009).
- 834 74. J. Alexander *et al.*, Development of high potency universal DR-restricted helper epitopes
835 by modification of high-affinity DR-blocking peptides. *Immunity* **1**, 751-761 (1994).
- 836 75. N. M. A. Okba *et al.*, Particulate multivalent presentation of the receptor binding domain
837 induces protective immune responses against MERS-CoV. *Emerg. Microbes Infect.* **9**,
838 1080-1091 (2020).
- 839 76. X. Ma *et al.*, Nanoparticle vaccines based on the receptor binding domain (RBD) and
840 heptad repeat (HR) of SARS-CoV-2 elicit robust protective immune responses. *Immunity*
841 **53**, 1315-1330.e1319 (2020).
- 842 77. A. C. Walls *et al.*, Elicitation of potent neutralizing antibody responses by designed
843 protein nanoparticle vaccines for SARS-CoV-2. *Cell* **183**, 1367-1382.e1317 (2020).
- 844 78. J. B. Bale *et al.*, Accurate design of megadalton-scale two-component icosahedral protein
845 complexes. *Science* **353**, 389-394 (2016).
- 846 79. J. Pallesen *et al.*, Immunogenicity and structures of a rationally designed prefusion
847 MERS-CoV spike antigen. *Proc. Natl. Acad. Sci. U. S. A.* **114**, E7348-E7357 (2017).
- 848 80. R. Henderson *et al.*, Controlling the SARS-CoV-2 spike glycoprotein conformation. *Nat.*
849 *Struct. Mol. Biol.* **27**, 925-933 (2020).
- 850 81. L. Kong *et al.*, Uncleaved prefusion-optimized gp140 trimers derived from analysis of
851 HIV-1 envelope metastability. *Nat. Commun.* **7**, 12040 (2016).
- 852 82. B. Zhang *et al.*, A platform incorporating trimeric antigens into self-assembling
853 nanoparticles reveals SARS-CoV-2-spike nanoparticles to elicit substantially higher
854 neutralizing responses than spike alone. *Sci. Rep.* **10**, 18149 (2020).
- 855 83. P. J. Hotez, D. B. Corry, U. Strych, M. E. Bottazzi, COVID-19 vaccines: Neutralizing
856 antibodies and the alum advantage. *Nat. Rev. Immunol.* **20**, 399-400 (2020).
- 857 84. K. H. D. Crawford *et al.*, Protocol and reagents for pseudotyping lentiviral particles with
858 SARS-CoV-2 spike protein for neutralization assays. *Viruses* **12**, 513 (2020).

- 859 85. E. S. Rosenberg *et al.*, Vigorous HIV-1-specific CD4(+) T cell responses associated with
860 control of viremia. *Science* **278**, 1447-1450 (1997).
- 861 86. L. M. Snell *et al.*, Overcoming CD4 Th1 cell fate restrictions to sustain antiviral CD8 T
862 cells and control persistent virus infection. *Cell Rep.* **16**, 3286-3296 (2016).
- 863 87. J. F. Zhu, H. Yamane, W. E. Paul, Differentiation of effector CD4 T cell populations.
864 *Annu. Rev. Immunol.* **28**, 445-489 (2010).
- 865 88. B. J. Laidlaw, J. E. Craft, S. M. Kaech, The multifaceted role of CD4(+) T cells in
866 CD8(+) T cell memory. *Nat. Rev. Immunol.* **16**, 102-111 (2016).
- 867 89. A. Grifoni *et al.*, Targets of T cell responses to SARS-CoV-2 coronavirus in humans with
868 COVID-19 disease and unexposed individuals. *Cell* **181**, 1489-1501.e1415 (2020).
- 869 90. M. Jeyanathan *et al.*, Immunological considerations for COVID-19 vaccine strategies
870 *Nat. Rev. Immunol.* **20**, 615-632 (2020).
- 871 91. Y. Peng *et al.*, Broad and strong memory CD4+ and CD8+ T cells induced by SARS-
872 CoV-2 in UK convalescent COVID-19 patients. *Nat. Immunol.* **21**, 1336-1345 (2020).
- 873 92. C. M. Krawczyk, H. Shen, E. J. Pearce, Functional plasticity in memory T helper cell
874 responses. *J. Immunol.* **178**, 4080-4088 (2007).
- 875 93. J. K. Taubenberger, D. M. Morens, 1918 influenza: the mother of all pandemics. *Emerg.*
876 *Infect. Dis.* **12**, 15-22 (2006).
- 877 94. K. P. O'Callaghan, A. M. Blatz, P. A. Offit, Developing a SARS-CoV-2 vaccine at warp
878 speed. *J. Am. Med. Assoc.* **324**, 437-438 (2020).
- 879 95. G. A. Poland, Tortoises, hares, and vaccines: A cautionary note for SARS-CoV-2 vaccine
880 development. *Vaccine* **38**, 4219-4220 (2020).
- 881 96. L. Corey, J. R. Mascola, A. S. Fauci, F. S. Collins, A strategic approach to COVID-19
882 vaccine R&D. *Science* **368**, 948-950 (2020).
- 883 97. M. S. Diamond, T. C. Pierson, The challenges of vaccine development against a new
884 virus during a pandemic. *Cell Host Microbe* **27**, 699-703 (2020).
- 885 98. G. Alter *et al.*, Whither COVID-19 vaccines? *Nat. Biotechnol.* **38**, 1132-1145 (2020).
- 886 99. J. P. Moore, P. J. Klasse, COVID-19 vaccines: "warp speed" needs mind melds, not
887 warped minds. *J. Virol.* **94**, e01083-01020 (2020).
- 888 100. K. Mochizuki *et al.*, Programming of donor T cells using allogeneic delta-like ligand 4-
889 positive dendritic cells to reduce GVHD in mice. *Blood* **127**, 3270-3280 (2016).

890
891 **Acknowledgements: Funding:** This work was funded by NIH Grants AI129698 and AI140844

892 (to J.Z.), Ufovax/SFP-2018-0416, Ufovax/SFP-2018-1013 and Ufovax/SFP-2020-0111 (to J.Z.).

893 **Author contributions:** Project design by L.H., Y.Z., I.A.W. and J.Z.; construct design of RBD

894 and spike-based immunogens by L.H. and J.Z.; plasmid design and processing by L.H. and C.S.;

895 antigen production, purification and basic characterization by L.H., X.L., and T.N.; antibody

896 production and column packing by L.H., X.L., and T.N.; antibody-antigen ELISA and BLI by

897 L.H. and C.S.; DSC by L.H. and J.Z.; negative-stain EM by L.H. and J.Z.; plasma-antigen

898 ELISA by L.H., X.L., and C.S.; antibody and mouse plasma neutralization by L.H. and X.L.;
899 vaccine-induced T-cell response analysis by Y.W., C.A., and Y.Z.; Manuscript written by L.H.,
900 Y.Z., I.A.W. and J.Z. All authors were asked to comment on the manuscript. The TSRI
901 manuscript number is 30028. **Competing interests:** Authors declare no competing interests.
902 **Data and materials availability:** All data are available in the main text or in the supplementary
903 materials. Additional data related to this paper may be requested from the corresponding author.

904

905 **Figure legends**

906 **Fig. 1. Rational design of SARS-CoV-1/2 RBD-based vaccines.** (A) Structural model of RBD-
907 5GS-1TD0 in an extended RBD-up conformation (top view and side view). 1TD0 is a
908 trimerization scaffold of viral origin. (B) SEC profiles of SARS-CoV-1/2 scaffolded RBD
909 trimers following ExpiCHO expression and CR3022 purification. (C) ELISA binding of SARS-
910 CoV-1/2 scaffolded RBD trimers to a panel of mAbs. EC₅₀ (μg/ml) values are labeled. (D) Octet
911 binding of the SARS-CoV-2 scaffolded RBD trimer to five mAbs. Sensorgrams were obtained
912 from an Octet RED96 instrument at six antigen concentrations from 950 to 29.5 nM by twofold
913 dilutions. (E) Diagram of conjugating RBD to the 24-meric FR SApNP using the
914 SpyTag/SpyCatcher (SPY) system. (F) SEC profiles of SARS-CoV-1/2 RBD-5GS-SPY-5GS-FR
915 SApNPs produced in ExpiCHO by co-expression (black line) and supernatant mix (red line). (G)
916 ELISA binding of SARS-CoV-1/2 RBD-FR SApNPs to a panel of mAbs. EC₅₀ (μg/ml) values
917 are labeled. (H) Octet binding of the SARS-CoV-2 RBD-FR SApNP to five mAbs. Sensorgrams
918 were obtained from an Octet RED96 instrument at six antigen concentrations from 37 to 1.1 nM
919 by twofold dilutions. (I) EM images of SARS-CoV-1 RBD-10GS-FR (gene fusion) and RBD-
920 5GS-SPY-5GS-FR (co-expression). (J) EM images of SARS-CoV-2 RBD-5GS-SPY-5GS-FR

921 produced by co-expression and supernatant mix. **(K)** Diagram of conjugating RBD to the 60-
922 meric multilayered I3-01v9 SApNP using the SPY system. Locking domains (LD) and T-helper
923 epitopes within the multilayered SApNP are depicted. **(L)** and **(M)** SEC profiles and EM images
924 of SARS-CoV-1/2 RBD-5GS-SPY-5GS-I3-01v9-LD7-PADRE (or I3-01v9-L7P) SApNPs
925 produced by supernatant mix. SEC profiles of scaffolded RBD trimers in (B) and SPY-linked
926 RBD SApNPs in (F) and (L) were obtained from a Superdex 200 10/300 GL column and a
927 Superose 6 10/300 GL column, respectively.

928 **Fig. 2. Rational design of SARS-CoV-2 spike antigens.** **(A)** Structural model of prefusion S
929 spike linked to the C-terminal trimerization domain (1TD0) with a 5GS linker in transparent
930 molecular surface. The approximate position for the unstructured HR2 stalk, or in this case a 5-
931 aa G₄S linker, is highlighted with a dashed line box. **(B)** SEC profiles of SARS-CoV-1 (top) and
932 SARS-CoV-2 (bottom) spikes. Left to right panels: S2P_{E_{CTO}}-5GS-1TD0 purified on Nickel and
933 CR3022 columns (1 and 2), S2G_{E_{CTO}}-5GS-1TD0 on Nickel and CR3022 columns (3 and 4), and
934 S2G Δ HR2-5GS-1TD0 on a CR3022 column (5). All spike constructs tested in (B) contain a C-
935 terminal His₆ tag to facilitate Nickel column purification. Results from three separate production
936 runs are shown for SARS-CoV-2 S2G_{E_{CTO}}-5GS-1TD0. **(C)** Schematic representation of a full-
937 length SARS-CoV-2 spike on the virus membrane surface in the presence of host ACE2 and the
938 HR2 region from a neighboring spike (left), and sequence alignment of SARS-CoV-1/2 HR1 and
939 HR2 regions (right, top and bottom). The HR1 and HR2 segments that form a six-helix bundle in
940 the post-fusion state are highlighted in green and brown shade, respectively. **(D)** Left: SEC
941 profiles of S2G Δ HR2-5GS-1TD0, showing results from four separate production runs. Right:
942 BN-PAGE analysis of S2P_{E_{CTO}}-5GS-1TD0 and S2G Δ HR2-5GS-1TD0. SEC fractions (12.5-
943 14.0) are shown for S2G Δ HR2-5GS-1TD0 on the gel. SEC profiles in (B) and (D) were obtained

944 from a Superose 6 10/300 GL column. **(E)** ELISA binding of two SARS-CoV-2 spikes
945 (S2P_{ECTO}-5GS-1TD0 and S2G Δ HR2-5GS-1TD0) to five mAbs. EC₅₀ (μ g/ml) values are labeled.
946 **(F)** Octet binding of two SARS-CoV-2 spikes (S2P_{ECTO}-5GS-1TD0 and S2G Δ HR2-5GS-1TD0)
947 to five mAbs. Sensorgrams were obtained from an Octet RED96 instrument at six antigen
948 concentrations from 150 to 4.7 nM by twofold dilutions. The spike constructs tested in (D)-(F)
949 do not contain a C-terminal His₆ tag.

950 **Fig. 3. Rational design of SARS-CoV-2 spike-presenting nanoparticle vaccines.** **(A)**
951 Schematic representation of SARS-CoV-2 virion (top) and spike-presenting SApNP vaccine
952 (bottom). For the SARS-CoV-2 virion, pre/post-fusion S, nucleocapsid, and RNA viral genome
953 are shown, while for the vaccine, stabilized spike and multilayered SApNP composition are
954 depicted. **(B)** Colored surface models of SApNP carriers (top) and spike-presenting SApNP
955 vaccines (bottom). The three SApNP carriers used here are ferritin (FR) 24-mer and multilayered
956 E2p and I3-01v9 60-mers (the LD layer and PADRE cluster are not shown). Particle size is
957 indicated by diameter (in nanometers). **(C)** SEC profiles of three SApNPs presenting the SARS-
958 CoV-2 S2G Δ HR2 spike, from left to right, S2G Δ HR2-5GS-FR, S2G Δ HR2-5GS-E2p-LD4-
959 PADRE (or E2p-L4P), and S2G Δ HR2-10GS-I3-01v9-LD7-PADRE (or I3-01v9-L7P). SEC
960 profiles were obtained from a Superose 6 10/300 GL column, each showing results from three
961 separate production runs. **(D)** EM images of three SARS-CoV-2 S2G Δ HR2 SApNPs. **(E)** ELISA
962 binding of three SARS-CoV-2 S2G Δ HR2 SApNPs to five mAbs. EC₅₀ (μ g/ml) values are
963 labeled. **(F)** Antigenic profiles of SARS-CoV-2 S2G Δ HR2 spike and three SApNPs against five
964 mAbs. Sensorgrams were obtained from an Octet RED96 using six antigen concentrations (150-
965 4.6 nM for spike, 9-0.27 nM for FR SApNP, and 3.5-0.1 nM for E2p and I3-01v9 SApNPs,
966 respectively, all by twofold dilutions) and AHQ biosensors, as shown in fig. S3B. The peak

967 binding signals (nm) at the highest concentration are listed. Color coding indicates the signal
968 strength measured by Octet (green to red: low to high).

969 **Fig. 4. SARS-CoV-1/2 vaccine-induced binding antibody (bAb) responses in BALB/c mice.**

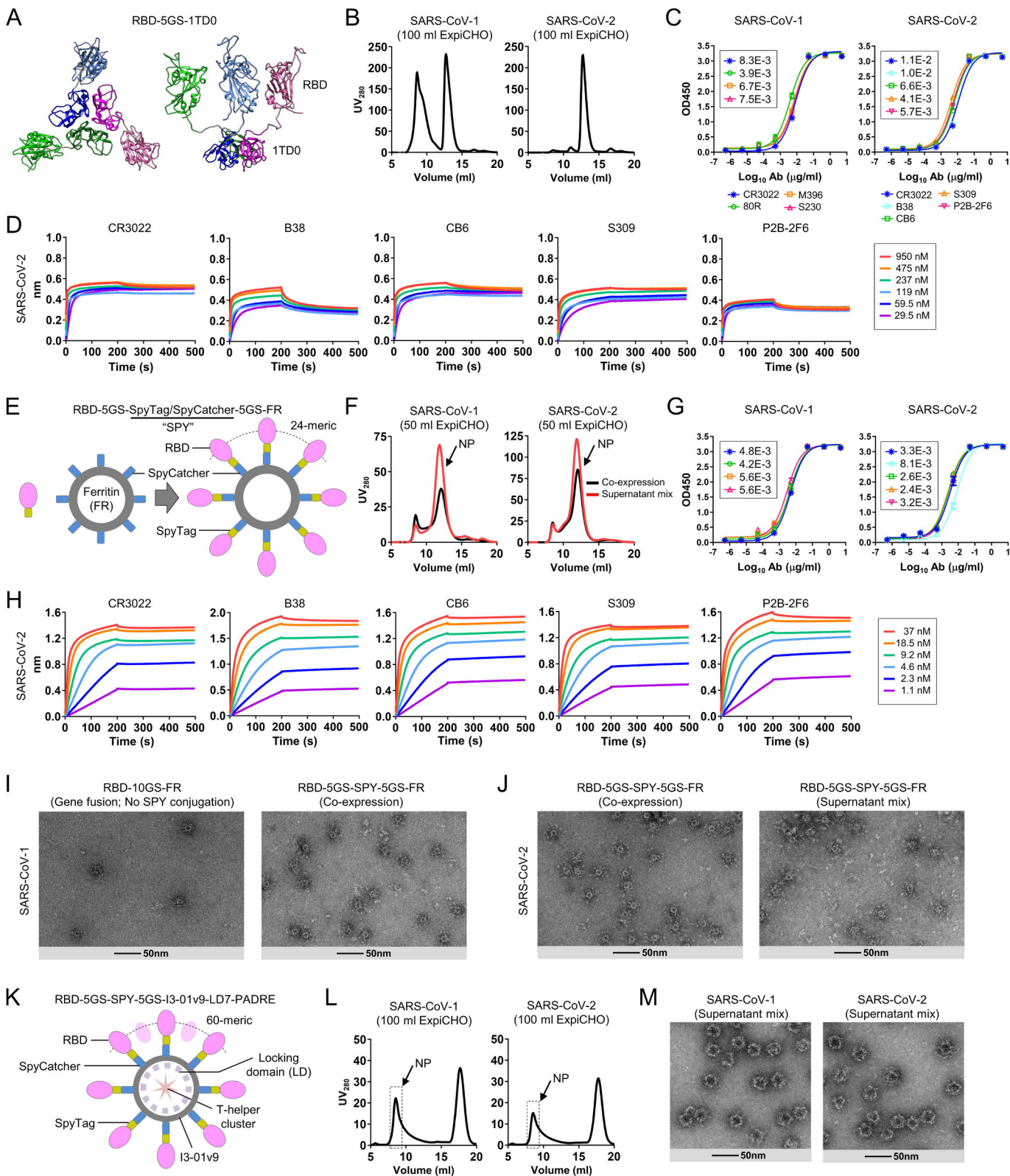
970 **(A)** Schematic representation of the mouse immunization protocol. **(B)** SARS-CoV-2 RBD and
971 RBD-SApNP vaccine-induced bAb responses. Coating antigens: SARS-CoV-2 S2GΔHR2-5GS-
972 foldon (left) and RBD (right). **(C)** SARS-CoV-2 S2GΔHR2 spike and S2GΔHR2-SApNP
973 vaccine-induced bAb responses. Coating antigens: SARS-CoV-2 S2GΔHR2-5GS-foldon (top)
974 and RBD (bottom). In (B) and (C), the SARS-CoV-2 S2P_{ECTO}-5GS-1TD0 group is included for
975 comparison, with S2P_{ECTO}-5GS-foldon used as the coating antigen. **(D)** SARS-CoV-1 RBD and
976 RBD-SApNP vaccine-induced bAb responses. Coating antigens: SARS-CoV-1 S2P_{ECTO}-5GS-
977 foldon (left) and RBD (right). In (D), the SARS-CoV-1 S2P_{ECTO}-5GS-1TD0 group is included
978 for comparison, with S2P_{ECTO}-5GS-foldon used as the coating antigen. In (B) to (D), EC₅₀ titers
979 derived from the ELISA binding of mouse plasma to coating antigens are plotted, with average
980 EC₅₀ values labeled on the plots. The *P* values were determined by an unpaired *t* test in
981 GraphPad Prism 8.4.3 with (*) indicating the level of statistical significance. Detailed ELISA
982 data are shown in figs. S4-S6.

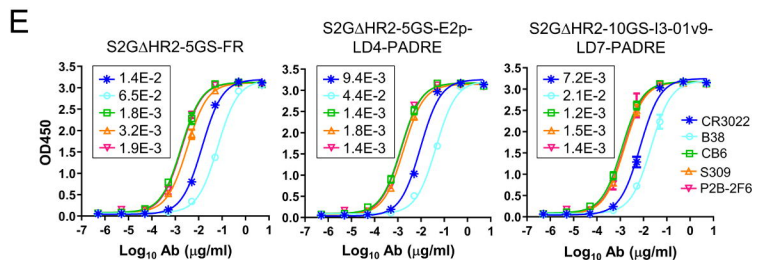
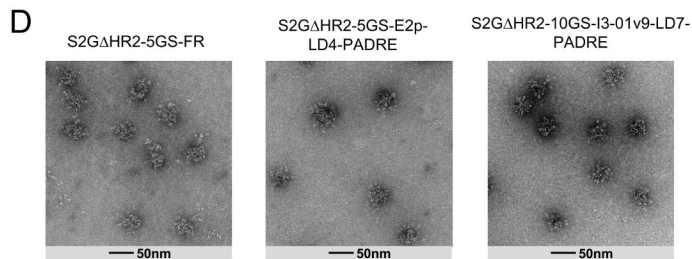
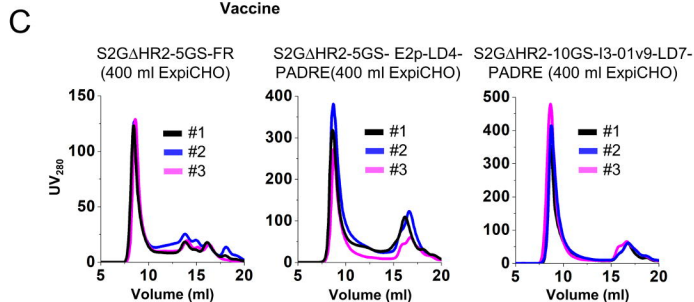
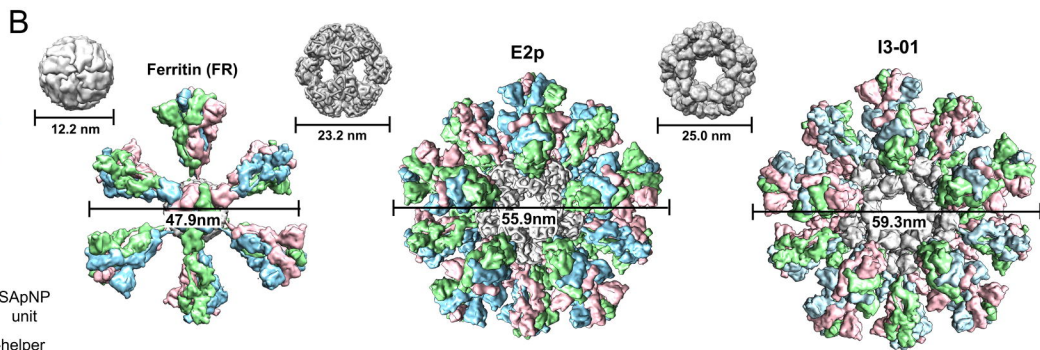
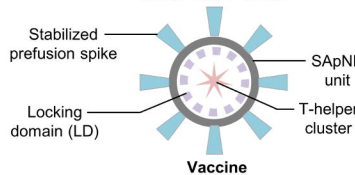
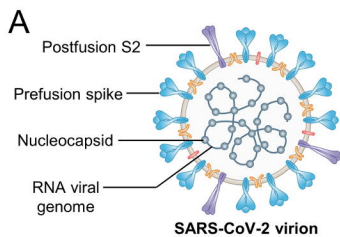
983 **Fig. 5. SARS-CoV-1/2 vaccine-induced neutralizing antibody (NAb) responses in BALB/c**

984 **mice.** **(A)** SARS-CoV-2 RBD and RBD-SApNP vaccine-induced NAb responses to autologous
985 SARS-CoV-2 (left) and heterologous SARS-CoV-1 (right). **(B)** SARS-CoV-2 S2GΔHR2 spike
986 and S2GΔHR2-SApNP vaccine-induced NAb responses to SARS-CoV-2 (top) and SARS-CoV-
987 1 (bottom). In (A) and (B), the SARS-CoV-2 S2P_{ECTO}-5GS-1TD0 group is included for
988 comparison. **(C)** SARS-CoV-1 RBD and RBD-SApNP vaccine-induced NAb responses to

989 autologous SARS-CoV-1 (left) and heterologous SARS-CoV-2 (right). In (C), the SARS-CoV-1
990 S2P_{ECTO}-5GS-1TD0 group is included for comparison. In (A) to (C), ID₅₀ titers derived from the
991 SARS-CoV-1/2-pp neutralization assays are plotted, with average ID₅₀ values labeled on the
992 plots. The *P* values were determined by an unpaired *t* test in GraphPad Prism 8.4.3 with (*)
993 indicating the level of statistical significance. Detailed SARS-CoV-1/2-pp neutralization data are
994 shown in figs. S7-S9.

995 **Fig. 6. SARS-CoV-2 vaccine-induced T-cell responses in BALB/c mice.** Splenocytes from
996 mice (n=5 in each group) immunized with S2P_{ECTO} spike, S2GΔHR2 E2p SApNP, and
997 S2GΔHR2 I3-01v9 SApNP, were isolated at w11 and cultured in the presence of IL-2 and
998 dendritic cells (DC) pulsed with S2P_{ECTO} (1×10^{-7} μM), S2GΔHR2 E2p (1×10^{-7} μM), and
999 S2GΔHR2 I3-01v9 (1×10^{-7} μM), respectively. Splenocytes from 5 naïve mice were used as
1000 control samples and cultured in the presence of DCs without antigen pulsing. Cells were assessed
1001 after 16 hours (A, C) and 4 hours (B, D) of culture. (A) and (B): Vaccine-induced CD4⁺ T cell
1002 immunity. (C) and (D): Vaccine-induced CD8⁺ T cell immunity. Plots show the frequencies of
1003 cell fraction. The *P* values were determined by one-way ANOVA analysis. *, *P* < 0.05; **, *P* <
1004 0.01; ***, *P* < 0.001.

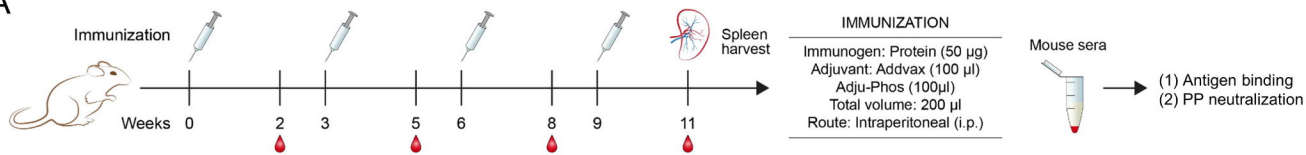
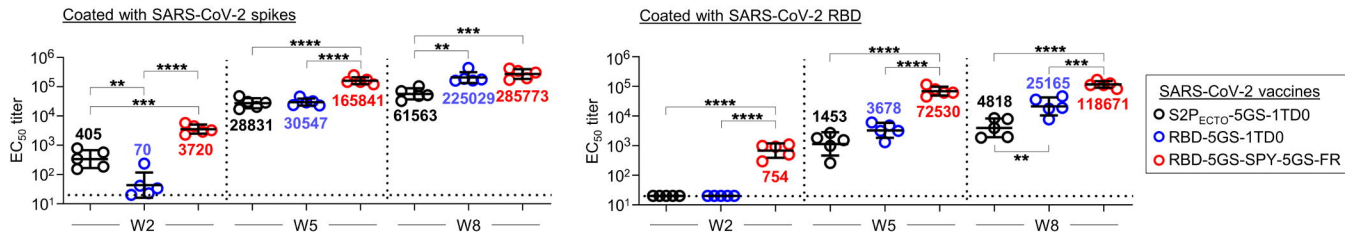
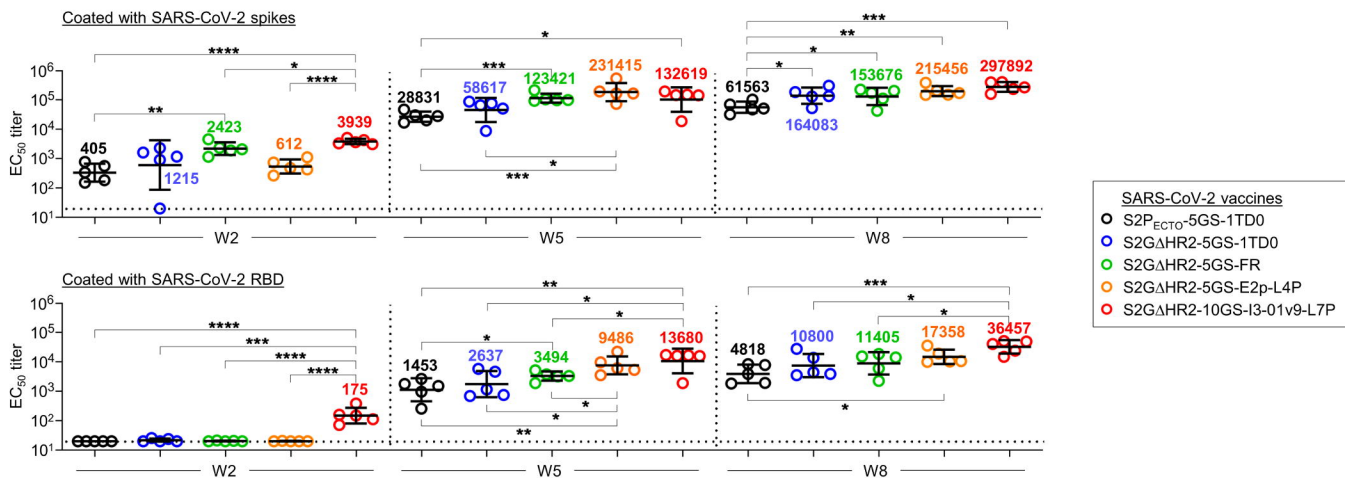
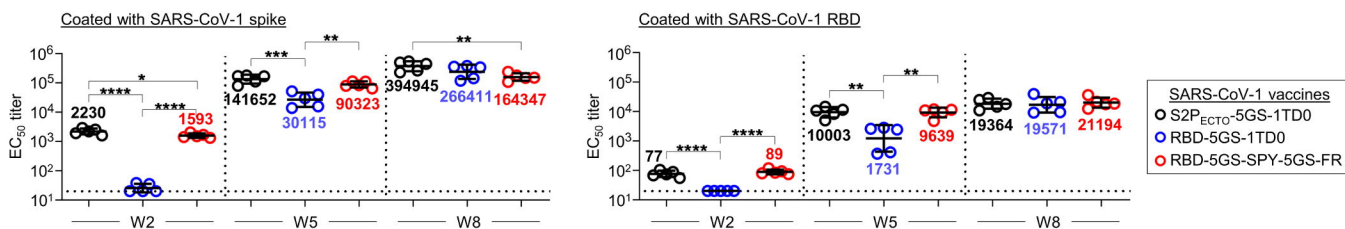




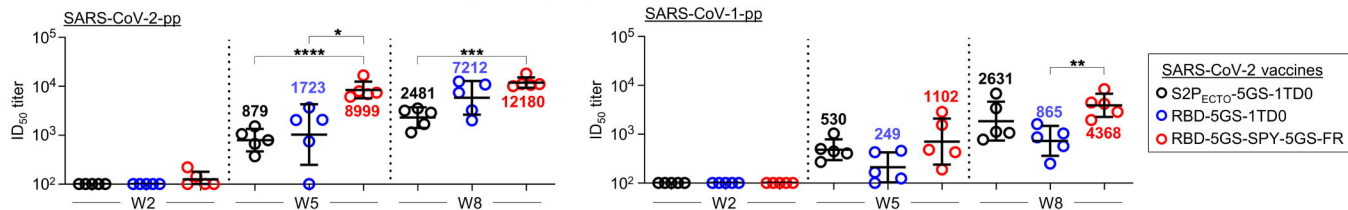
F

SARS-CoV-2 S constructs

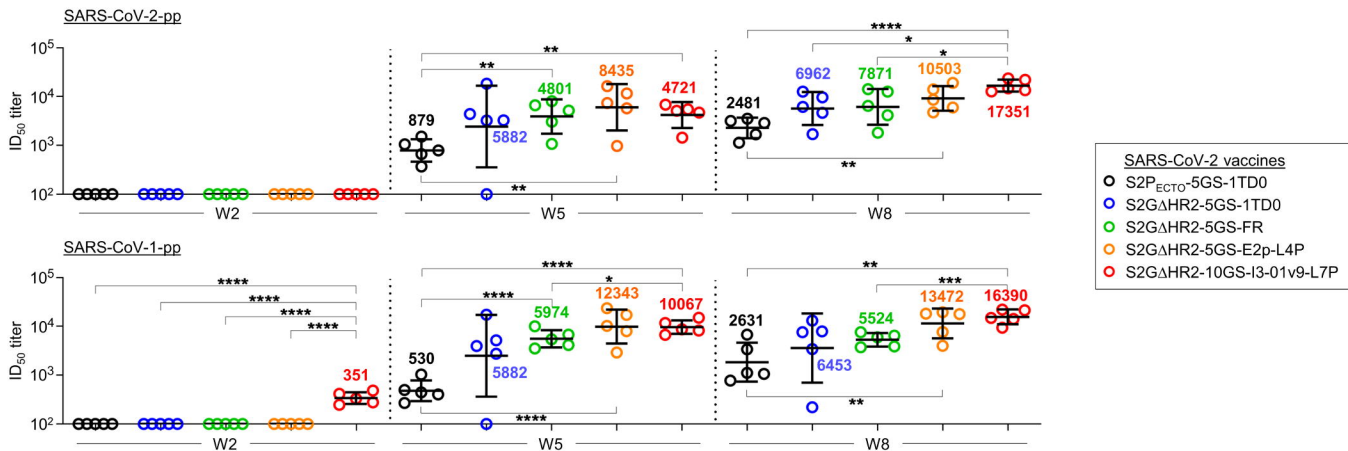
	CR3022	B38	CB6	S309	P2B-2F6
S2G Δ HR2-5GS-1TD0	1.17	1.07	0.83	0.94	0.77
S2G Δ HR2-5GS-FR	1.12	1.41	1.27	1.06	1.68
S2G Δ HR2-5GS-E2p-LD4-PADRE	1.92	2.27	1.82	1.67	1.98
S2G Δ HR2-10GS-I3-01v9-LD7-PADRE	1.93	1.99	1.93	1.73	1.92

A**B****SARS-CoV-2 RBD-based vaccine-induced binding antibody responses****C****SARS-CoV-2 spike-based vaccine-induced binding antibody responses****D****SARS-CoV-1 vaccine-induced binding antibody responses**

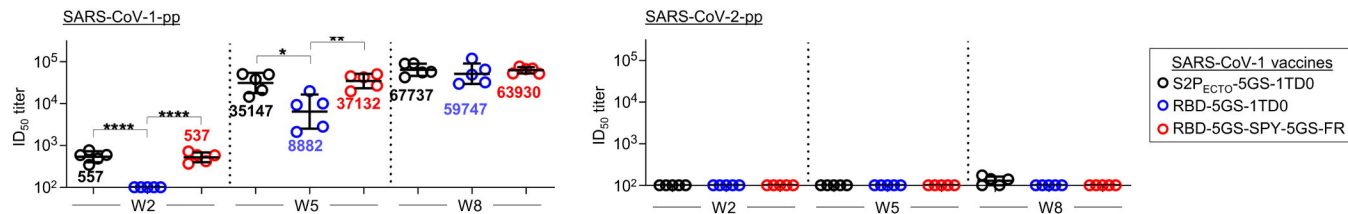
A SARS-CoV-2 RBD-based vaccine-induced neutralizing antibody responses



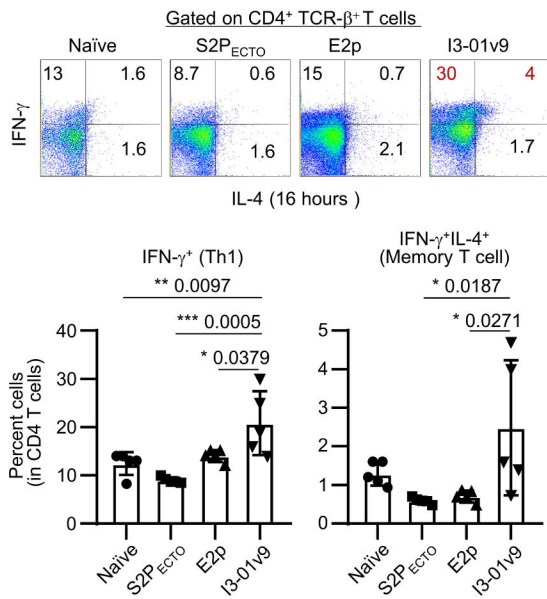
B SARS-CoV-2 spike-based vaccine-induced neutralizing antibody responses



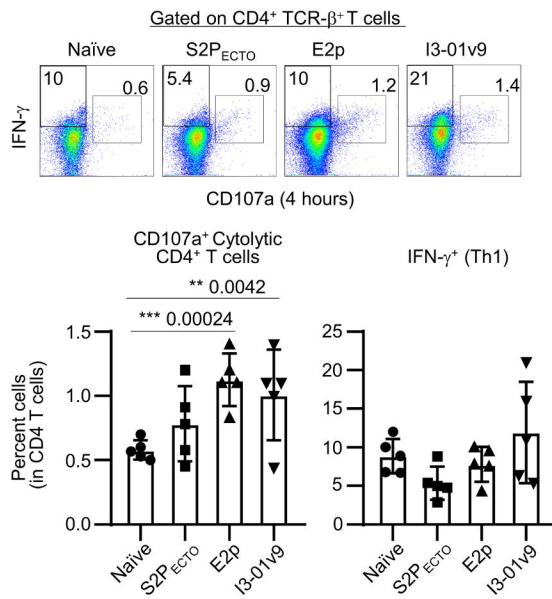
C SARS-CoV-1 vaccine-induced neutralizing antibody responses



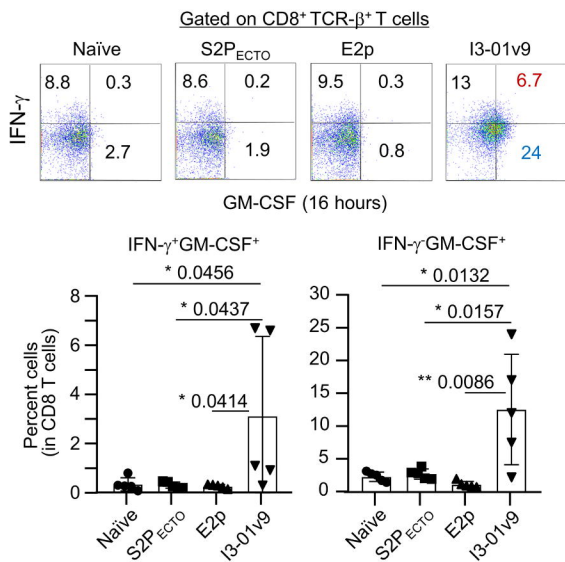
A Induction of Th1 and memory responses



B Induction of cytolytic CD4⁺ T cells



C Induction of recall response of CD8⁺ T cells



D Induction of rapid CD8⁺ T cell recall response

